

A TIME-DEPENDENT DIRECT SAMPLING METHOD FOR RECOVERING MOVING POTENTIALS IN A HEAT EQUATION*

YAT TIN CHOW[†], KAZUFUMI ITO[‡], AND JUN ZOU[§]

Abstract. We are concerned with a numerical reconstruction of the moving potential/absorption coefficient in a heat conduction process when only a single set of boundary measurements of the thermal reflection is available. We propose an efficient direct sampling method (DSM) to locate moving extended objects, represented by time-dependent potentials in a heat equation, and track the trajectories of the moving objects. This appears to be the first DSM for recovering and tracking moving inhomogeneous inclusions in a time-dependent PDE system. Our new method is essentially different from the existing DSMs for solving various stationary or time-harmonic inverse problems but still preserves several important features: it is robust against the noise in the data, easy to implement, and inexpensive computationally. Mathematical justifications are provided to verify the validity of this new method, and insightful mathematical analysis is performed to understand the behavior of the key probing functions proposed. Numerical experiments are presented to demonstrate the effectiveness and efficiency of the method. The DSM provides a new promising numerical strategy for the ill-posed inverse problem of recovering time-dependent moving inhomogeneous media.

Key words. time-dependent direct sampling method, inverse heat equation, diffusive optical tomography, moving potential reconstruction, inverse problems

AMS subject classifications. 35K20, 35R30, 60J60, 65N21, 76R50, 78A70, 80A23

DOI. 10.1137/16M1090831

1. Introduction. In this work we develop a novel direct sampling method (DSM) for recovering the time-dependent potential/absorption coefficient in a heat conduction process. The model used here may also be used as the model for other important applications, such as the photon migration in the time-dependent diffusive optical tomography (DOT) [1, 2, 8, 14]. We consider a homogeneous background absorption medium space \mathbb{R}^2 , with the constant conductivity a and a background absorption coefficient/potential q_0 . Let Ω be an open bounded connected domain with a piecewise C^2 boundary sitting inside the homogeneous background medium space. Suppose that $q \in L^\infty(\mathbb{R}^2 \times (0, T))$ is a nonnegative function representing the potential/absorption coefficient. We shall often write the support of $q - q_0$ as $D(t)$ at time t , which represents the moving inhomogeneous inclusions and is assumed to sit inside Ω . We consider the following heat equation model that governs the behavior of the heat

*Submitted to the journal's Methods and Algorithms for Scientific Computing section August 23, 2016; accepted for publication (in revised form) June 14, 2018; published electronically August 30, 2018.

<http://www.siam.org/journals/sisc/40-4/M109083.html>

Funding: The first author's research was partially supported by NSF grant ECCS-1462398 and ONR grant N000141410683. The third author's research was substantially supported by a Hong Kong RGC grant (project 14322516) and a direct grant for research from The Chinese University of Hong Kong.

[†]Department of Mathematics, University of California, Riverside, CA 92521 (ytchow@math.ucla.edu).

[‡]Department of Mathematics and Center for Research in Scientific Computation, North Carolina State University, Raleigh, NC 27695-8212 (kito@unity.ncsu.edu).

[§]Department of Mathematics, The Chinese University of Hong Kong, Shatin, N.T., Hong Kong (zou@math.cuhk.edu.hk).

intensity u :

$$(1.1) \quad \begin{cases} \frac{\partial u}{\partial t} = a \Delta u - q u & \text{in } \mathbb{R}^2 \times (0, T), \\ u(x, 0) = u_0(x) & \text{on } \mathbb{R}^2, \\ u \text{ decays as } |x| \rightarrow \infty, \end{cases}$$

with $u \in L^2(0, T; H_0^1(\mathbb{R}^2))$ and $\frac{\partial u}{\partial t} \in L^2(0, T; H^{-1}(\mathbb{R}^2))$. We assume the potential q of the form

$$(1.2) \quad q(x, t) := \sum_{i=1}^k q(x - \gamma_i(t)),$$

where $\gamma_i \in C^1((0, T); \Omega)$ are some smooth curves inside Ω such that the support of $q - q_0$ sits inside Ω for $1 \leq i \leq k$.

For the sake of exposition, a special potential q of the form

$$(1.3) \quad q(x, t) = q_0 + \sum_{i=1}^k (q_i - q_0) \chi_{B_i}(x - \gamma_i(t))$$

is considered, where B_1, \dots, B_k are open connected subdomains in Ω , q_1, \dots, q_k are positive constants, and each γ_i represents the moving path of object B_i inside Ω .

Assume that for a fixed given initial datum u_0 , we assume a single measurement of the heat intensity $u(\cdot, \cdot)$ along $\Gamma \times (0, T) = \partial\Omega \times (0, T)$, where $\Gamma = \partial\Omega$ is the measurement surface of the sampling domain Ω . Here and throughout the paper, we shall often write the heat intensity over $\Gamma \times (0, T)$ as f , i.e., $f := u|_{\Gamma \times (0, T)}$. Our inverse medium problem is then formulated as follows: given ONE single measurement f , we recover the locations and the number of inhomogeneities $D(t)$ inside the homogeneous background medium along with time and therefore track the movement of the inhomogeneous objects in Ω . We would like to emphasize that we make use of only a single set of measurement data, i.e., the data $f = u|_{\Gamma \times (0, T)}$ taken over $\Gamma \times (0, T)$ for a single initial value u_0 . This is a highly challenging but very important situation in applications.

It is well known that a time-dependent potential $q(x, t)$ can be uniquely determined by the full lateral Dirichlet-to-Neumann map, i.e., $\Lambda : (u(\cdot, 0), u|_{\Gamma \times (0, T)}) \mapsto (u(\cdot, T), \partial_n u|_{\Gamma \times (0, T)})$ [3, 4, 6, 16, 17, 22, 24]. Some numerical reconstruction methods were proposed in these references for recovering q from the full Dirichlet-to-Neumann map, but their computational efforts are tremendous and may also not be practical for applications. In [10], the recovery of a time-independent coefficient in a one-dimensional heat equation was shown to be unique from a finite set of Dirichlet-to-Neumann measurements on the boundary.

In this work, we propose a DSM for the inverse medium problem we stated above, i.e., recovering the moving potential of form (1.3) from a single measurement f on the measurement surface Γ . We will propose a new set of probing functions and then use these probing functions to define a new family of index functions $I_\gamma^\alpha(x, t)$ to recover the locations of $D(t)$ inside Ω along with time t . From this family of index functions, we can determine the number and locations of inhomogeneous inclusions effectively and track the movement of the inclusions.

One point to note is that, from the definition of our probing functions and newly proposed index function, the value of an index function at a point (x, t) has nothing to

do with the measurements $f(\cdot, s)$ for $s > t$, and therefore the index can be computed in real time, frame by frame. This is a clear advantage of our method when one hopes to image real-time movements of objects and inclusions.

This new DSM is essentially different from the existing DSMs that have been developed, e.g., in [11, 12, 19, 20, 21, 23], for recovering the stationary inclusions; it has several novel features and brings the family of DSMs to a new stage of development. First of all, our new family of probing functions in this work involves high-order derivatives of the fundamental solutions inside the domain Ω , which is completely different from those generated by monopoles/dipoles/multipoles in our previous works and therefore much easier to compute.

We notice that, from the definition of our probing functions and newly proposed index function, the index can be computed in real time, frame by frame.

Then, in order to increase the sharpness and eliminate the deficiencies of the index functions for locating inhomogeneities, we take (temporal) derivatives of the index functions to generate a family of higher-order index functions, which are still easy to evaluate. This is quite contrary to the previous approaches in the development of DSMs, where the sharpness and sensitivity of the indices are increased by adjusting their Sobolev scales in the duality products and weighting. Furthermore, we notice that our new method takes a forward-projection strategy, deviated essentially from the usual back-projection or time reversal strategy, as developed in the existing literature either by ourselves or others. All these new features make it possible to reconstruct moving inhomogeneous inclusions in an efficient and robust manner, as demonstrated systematically in the subsequent sections.

The rest of the paper is organized as follows. In section 2, we introduce the general philosophy of the DSM as well as the properties of probing and index functions that we need to recover the moving potential q in (1.3). Then we devote section 3 to the major development of this work. We first construct the probing and index functions in sections 3.2 and 3.3, which are followed by an introduction of high-order index functions in section 3.4 by taking temporal derivatives. Mathematical and graphic justifications are then given in section 3.6 for the effectiveness of the index functions, and some further analysis is provided in section 3.7 to help us better understand the behavior of these index functions and to verify the enhancement of the contrast of the index functions by an increase of the temporal derivatives of the indices. We then provide an alternative characterization of our index functions and explain the concept of our forward-projection method, which is, to the best of our knowledge, completely new in terms of the solution of inverse problems. Some detailed strategies for numerical implementations are given in section 4 to increase the stability and robustness of our method, including a nonlinear mollification process of index functions based on a fading memory technique, a prior-corrected trajectory identification, and an appropriately selected regularization of the trajectory of the moving objects. Numerical results are presented in section 5 to demonstrate the effectiveness and robustness of the new DSM for recovering one or two moving objects.

2. Principles of the time-dependent direct sampling method. In this section, we shall give a brief introduction to the general philosophy of our new time-dependent DSM. The existing DSMs are a family of simple and efficient inversion methods that aim at providing a good estimate of the locations of inhomogeneities inside a homogeneous background representing various physical media from a single or a small number of boundary data in both full and limited aperture cases. They were introduced and studied in [21, 23] using far-field data and in [20] using near-field data

for locating inhomogeneities in inverse acoustic medium scattering. The method is based on the well-known fact that the scattered field can be approximated by a finite sum of the fundamental solutions centered at the inhomogeneous scatterers. With the help of a family of probing functions that are nearly orthogonal in some inner product space, an index function can be defined in such a way that it attains large values inside the inhomogeneous scatterers but small values outside. This index function has been shown to be a very effective tool for reconstructing extended scatterers in two- and three-dimensional scattering media with a limited number of incident plane waves. It was later extended to various other coefficient determination inverse problems, such as electrical impedance tomography (EIT) [12], diffusive optical tomography (DOT) [11], and the electromagnetic inverse scattering problem [19]. In each of the aforementioned tomographies, a family of probing functions is introduced and an index function is defined as a dual product between the observed data and the probing function under an appropriate choice of Sobolev scale. The evaluation of the index function is very efficient computationally, and the images obtained from the index functions are proven to be effective in locating inhomogeneous inclusions. For more details about the existing DSMs for locating stationary inhomogeneous inclusions, we refer the reader to [2, 11, 12, 19, 20, 21, 23].

In this work, we develop a novel DSM for solving a time-dependent inverse problem, namely identifying the potential in a heat conductive system, for which we propose a new important family of probing functions and index functions.

In what follows, we derive a general framework of the DSM for an inverse heat equation. Consider u as the total heat intensity that is the solution to (1.1). We shall often write u_0 as the heat intensity with homogeneous background potential, i.e., the solution to (1.1) with $q = q_0$. Then we can easily see that

$$(2.1) \quad \begin{cases} \frac{\partial(u - u_0)}{\partial t} - a\Delta(u - u_0) = -q_0(u - u_0) - (q - q_0)u & \text{in } \mathbb{R}^2 \times (0, T), \\ (u - u_0)(x, 0) = 0 & \text{on } \mathbb{R}^2, \\ u - u_0 \text{ decays as } |x| \rightarrow \infty. \end{cases}$$

If we define $c(y, s) := (q(y, s) - q_0(y, s))u(y, s)$, then for the moving potential (1.3) with $q_0 = 0$ we have

$$c(y, s) = \sum_{i=1}^k q_i \chi_{B_i}(y - \Gamma_i(s)) u(y, s).$$

Now we infer from the Green's formula that

$$(2.2) \quad (u - u_0)(x, t) = - \int_0^t \int_{\mathbb{R}^2} \Phi(x - y, t - s) c(y, s) dy ds = - \int_0^T \int_{D(t)} \Phi(x - y, t - s) c(y, s) dy ds,$$

where Φ is the fundamental solution to the heat equation given by

$$(2.3) \quad \Phi(x, t) = \chi_{t>0}(t) \frac{1}{4\pi at} \exp\left(-\frac{|x|^2}{4at}\right).$$

Applying a general quadrature rule for (2.2), we can approximate the scattered potential $f - f_0 := (u - u_0)|_{\Gamma \times (0, T)}$ by a finite sum of fundamental solutions in the following form:

$$(2.4) \quad (f - f_0)(\xi, t) \approx \sum_{k,j} c_{kj} \Phi(\xi - y_k, t - s_j), \quad (\xi, t) \in \Gamma \times (0, T),$$

where $\{(y_k, s_j)\}$ are quadrature points located inside $\cup_{t \in (0, T)} D(t)$ and $\{c_{kj}\}$ are weight coefficients in space and time.

If we can define a family of probing functions $\{\eta_{x,t}\}_{x \in \Omega, t \in (0, T)} \subset L^2(\Gamma \times (0, T))$ such that they are nearly orthogonal to the family $\{\Phi_{y,s} := \Phi(y - \cdot, s - \cdot) |_{\Gamma}\}_{y \in \Omega, s \in (0, T)}$ with respect to a semi-inner product $\langle \cdot, \cdot \rangle_X$ in a Hilbert space X and a seminorm $|\cdot|_Y$ in a Hilbert space Y in the following sense, namely for any $(y, s) \in \Omega \times (0, T)$, the function

$$(2.5) \quad (x, t) \mapsto K_0(x, y; t, s) := \frac{\langle \eta_{x,t}, \Phi_{y,s} \rangle_X}{|\eta_{x,t}|_Y}, \quad (x, t) \in \Omega \times (0, T),$$

attains the maximum at $(x, t) = (y, s)$ and decays when (x, t) moves away from (y, s) .

Now if we define an index function

$$(2.6) \quad I_0(x, t) := \frac{\langle \eta_{x,t}, f - f_0 \rangle_X}{|\eta_{x,t}|_Y}, \quad (x, t) \in \Omega \times (0, T),$$

then by substituting (2.4) into (2.6), we arrive at

$$(2.7) \quad I_0(x, t) = \frac{\langle \eta_{x,t}, f - f_0 \rangle_X}{|\eta_{x,t}|_Y} \approx \sum_{k,j} c_{kj} \frac{\langle \eta_{x,t}, \Phi_{y_k, s_j} \rangle_X}{|\eta_{x,t}|_Y} = \sum_{k,j} c_{kj} K_0(x, y_k; t, s_j).$$

From the representation (2.7) of the index function I_0 , we can see that the magnitude of I_0 is relatively large inside $\cup_{t \in (0, T)} D(t) \subset (0, T) \times \Omega$, and it is relatively small outside; see numerical verifications in section 3.4 and mathematical justifications in sections 3.6–3.8. Therefore, if the magnitude of the index function I_0 is relatively large at a point (x, t) in space and time, it is most likely that the point x lies inside $\cup_{t \in (0, T)} D(t)$. On the contrary, if the magnitude of I_0 is relatively small at (x, t) , it is then very likely that the point is at the homogeneous background. Therefore, the index function provides us with an estimate of the time-dependent location of $D(t)$ and hence also the number of and moving trajectories of the inhomogeneous inclusions.

The above description gives only a general principle of our DSM to recover the location of $D(t)$, based on the index function $I_0(x, t)$ in (2.6). But, for the implementation of the DSM, we have to compute $I_0(x, t)$ at each selected sampling point and time (x_k, t_j) in $\Omega \times (0, T)$, for which we need the measurement data $f - f_0$ on $\Gamma \times (0, T)$ and the explicit expressions of the probing functions $\{\eta_{x_k, t_j}\}$ over $\Gamma \times (0, T)$. So it is more convenient for us to present the detailed implementations of the DSM in later sections, after our further discussions about the choices of probing functions and several variants of the index function $I_0(x, t)$; see sections 3.5 and 4.1 for Algorithms I and II, respectively.

3. Time-dependent probing and index functions.

3.1. New features of time-dependent DSM. In the previous section, we introduced the basic concept of the time-dependent DSM and applied this concept to the moving potential identification in the heat equation. As we shall see in the subsequent development, the new time-dependent DSM is essentially different from the previous DSMs [11, 12, 19, 20, 21, 23].

First, instead of using a family of probing functions generated by monopoles/dipoles/multiples, as developed in [11, 12, 19, 20, 21, 23], our new family of probing functions (cf. section 3.2) is a high-order derivative of a family of fundamental solutions taken inside the domain Ω . This makes the family of probing functions easier to evaluate.

Second, all the existing DSMs increase the sharpness and sensitivity of the index function by adjusting their Sobolev scales in the corresponding duality products and weighting involved. But, as we will see later in section 3.3, this conventional strategy for DSMs does not work effectively for locating time-dependent inclusions. Instead, we find it much more effective to take the (temporal) derivatives of our new index functions to generate a family of higher-order index functions, which are shown to be able to enhance the sharpness and eliminate the deficiencies of locating the inhomogeneities, as developed in sections 3.6–3.7. The resulting index functions are still cheap to compute and will be also shown to be efficient and robust for our desired moving potential identification.

Moreover, we would like to emphasize that, with the new probing functions, the time-dependent DSM does not involve a usual back-projection or time reversal strategy as it did in all the existing DSMs for various stationary or time-harmonic inverse problems. Instead, it can be illustrated well using a novel efficient forward-projection strategy (cf. section 3.3), as done in depth in section 3.8.

3.2. Probing functions. We are now ready to introduce an appropriate family of time-dependent probing functions $\{\eta_{x,t}\}$, which will be used for our DSM for the moving potential identification in the heat equation.

With a given small $\delta > 0$ and $\alpha \in \mathbb{N}$, for any given point y in Ω and time $s \in (0, T)$, we define an auxiliary function $w_{y,s}^\alpha$:

$$(3.1) \quad w_{y,s}^\alpha(x, t) = \Delta_x^\alpha \Phi_{y,s}(x, t) \chi_{\mathbb{R}^+}(s - t - \delta), \quad (x, t) \in \Omega \times (0, T).$$

Then we define a family of probing functions $\{\eta_{y,s}^\alpha\}_{y \in \Omega, s \in (0, T)}$ as the trace of the family of the auxiliary functions on $\Gamma \times (0, T)$, i.e.,

$$(3.2) \quad \eta_{y,s}^\alpha = w_{y,s}^\alpha|_{\Gamma \times (0, T)}.$$

We would like to remark that the introduction of a cut-off parameter δ in the time direction is only for removing a possible blowup at $t = s$ when the sampling point $y \in \Omega$ approaches the function argument x on the boundary Γ and hence to ensure the numerical stability in the implementation of the desired DSM.

As one can clearly see, our family of probing functions is the boundary data of the fundamental solutions after taking a 2α -order derivative inside the domain. It is quite different from the monopoles or dipoles as used in the previous DSMs for solving other medium inverse problems; see, e.g., [11, 12, 19, 20, 21, 23].

3.3. Zeroth-order index function. With the probing functions $\eta_{x,t}^\alpha$ introduced in the previous subsection, we now discuss an appropriate choice of two Hilbert spaces X and Y for our time-dependent (zeroth-order) index function I_0^α .

For the definition of the index function I_0^α , we first consider both the semi-inner product and the seminorm from the special space $X = Y = L^2(\Gamma \times (0, T))$. Therefore, the index function in (2.6) reads as

$$(3.3) \quad I_0^\alpha(x, t) := \frac{\langle \eta_{x,t}^\alpha, f - f_0 \rangle_{L^2(\Gamma \times (0, T))}}{|\eta_{x,t}^\alpha|_{L^2(\Gamma \times (0, T))}} = \frac{\int_0^{t-\delta} \int_\Gamma \eta_{x,t}^\alpha(p, r) (f - f_0)(p, r) dp dr}{|\eta_{x,t}^\alpha|_{L^2(\Gamma \times (0, T))}}, \quad (x, t) \in \Omega \times (0, T).$$

We would like to remark again that the value of $f(\cdot, \cdot) = u(\cdot, \cdot)|_{\partial\Omega \times (0, T)}$ is one single measurement on $\partial\Omega \times (0, T)$. This one measurement event at the boundary can be realized by taking $u(x_i, t_j)$, where $(x_i, t_j) \in \Gamma \times (0, T)$ are some mesh points.

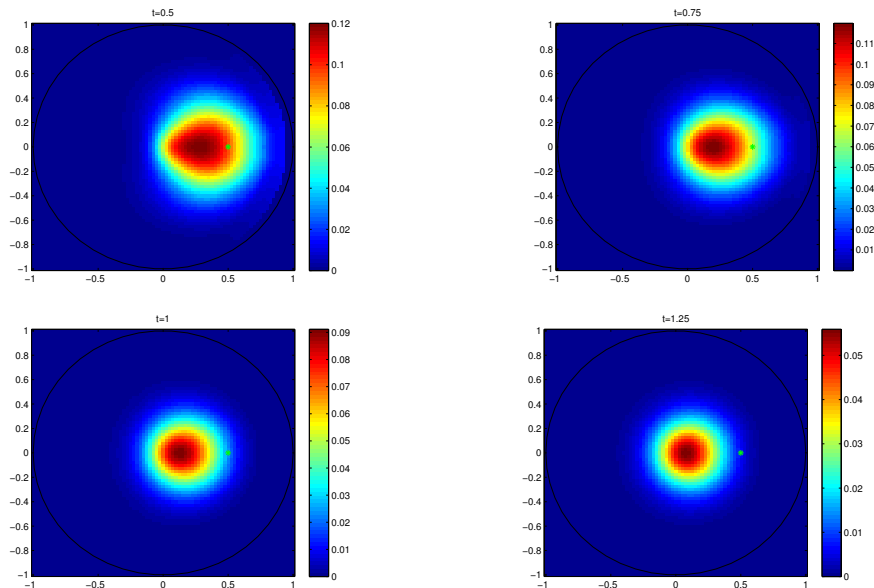


FIG. 1. $I_0^\alpha(\cdot, t)$ for $t = 0.5, 0.75, 1.0, 1.25$ and $\alpha = 2$, with the scattered field by the point potential $q = \delta_{(0.5,0)}(x)\delta_1(t)$ at the point $(0.5, 0)$ marked by a green star. The maximum in each graph is either 0.120, 0.119, 0.091, or 0.055 (round to three decimal places). Color is available online only.

For a better illustrative purpose and comparison at each time t , we normalize the index by a constant such that the maximum of the index values is 1:

$$(3.4) \quad \hat{I}_0^\alpha(x, t) = \frac{|I_0^\alpha(x, t)|}{\max_{x \in \Omega} |I_0^\alpha(x, t)|}.$$

One point to notice is that, by the definition of our probing functions, to compute a value $I_0^\alpha(x, t)$, we actually do not need to use any information about $f(\cdot, s)$ for $s > t$. Therefore, the computation can be done in real time, frame by frame. This is a clear advantage of our method.

To emphasize the dependence of K_0 in (2.5) on α , we shall write K_0 as K_0^α from now on. For a better understanding of the performance of the above zeroth-order index function, Figure 1 shows the value of the kernel $K_0^\alpha(x, (0.5, 0); t, 1)$ at $t = 0.5, 0.75, 1.0, 1.25$ for $\alpha = 2$. It can also be regarded as the index function I_0^α of the scattered field by a point potential $q = \delta_{(0.5,0)}(x)\delta_1(t)$.

To illustrate how the kernel changes over the temporal parameter, let us note that the maximum in each graph for $t = 0.5, 0.75, 1.0, 1.25$ is either 0.120, 0.119, 0.091, or 0.055 (round to three decimal places).

From the four plots in Figure 1, we can clearly see that there are two disappointing deficiencies in the index function I_0^α . First of all, the probing function does not appear to be sensitive with respect to the time. And we can see that it is also inaccurate in time, as the spatial maxima do not occur at the desired locations; in fact, they are actually shifted toward the origin instead. These observations are not only related to the very ill posed nature of the concerned inverse problem but are also closely related to the fact that the zeroth-order index I_0^α has some inherent deficiencies, as will be

further discussed in sections 3.6–3.7. Therefore, I_0^α is generally not a good candidate for the purpose of an index function to locate the moving inclusion $\cup_{t \in [0, T]} (D(t), t)$.

In the next subsection, we propose a new family of (higher-order) index functions I_γ^α derived from I_0^α , which can yield an improved index function that achieves more accurate space-time locations as γ increases (up to α).

3.4. Temporal derivatives and a new family of higher-order index functions. From the previous subsection, we observe that the index function I_0^α is neither sharp nor accurate in locating the movement of the inclusions: it does not give a temporal local maximum as we hoped it would have, and it is not sharp in space such that the spatial maximum of the index function, though near the true location, always deviates from it by a considerable distance. In this subsection, we would like to propose a new family of higher-order index functions I_γ^α derived from I_0^α , which shall enhance the performance of the zero-order index.

Motivated by our previous observations, we shall introduce the higher-order index functions by taking the time derivatives of the zero-order index I_0^α . Indeed, from the behavior of the kernel function K_0^α in Figure 1, we notice that the spatial maximum starts to drop quite significantly with respect to time as time goes over from $t = 1$ onward. Therefore, we expect that a rate of change of the deficient index function I_0^α may capture the inclusion bulk more effectively.

With this observation, we now introduce the following modification by defining a modified index I_1^α as the temporal derivative of the index I_0^α , i.e.,

$$(3.5) \quad I_1^\alpha = \frac{\partial}{\partial t} I_0^\alpha.$$

Again, for a better illustrative purpose and comparison, we shall normalize this new index:

$$(3.6) \quad \hat{I}_1^\alpha(x, t) = \frac{|I_1^\alpha(x, t)|}{\max_{x \in \Omega} |I_1^\alpha(x, t)|}.$$

For a better understanding of the performance of our newly introduced first-order index function, Figure 2 shows the value of the kernel $I_\gamma^\alpha(\cdot, t)$ at $t = 0.5, 0.75, 1.0, 1.25$, with a point potential $q = \delta_{(0.5, 0)}(x)\delta_1(t)$ and $\alpha = 2, \gamma = 1$. To illustrate how the kernel changes over the temporal parameter, we may note that the maximum in the graphs for $t = 0.5, 0.75, 1.0, 1.25$ is either 0.027, 0.026, 0.031, or 0.002.

We may easily observe from Figure 2 that the new first-order index function I_1^2 provides a much sharper location of the inclusion in both space and time than I_0^2 (cf. Figure 1). First, Figure 1 indicates that the maximum of $K_0^2(x, (0.5, 0); t, 1)$ at time $t = 1$ deviates significantly from the target point $(0.5, 0)$, while Figure 2 shows that the maximum of $K_1^2(x, (0.5, 0); t, 1)$ at time $t = 1$ is attained at a point very close to the target $(0.5, 0)$. Second, the temporal sensitivity of I_1^2 also outperforms I_0^2 . In fact, we see from Figure 1 that the temporal maximum of the function $K_0^2(x, (0.5, 0); t, 1)$ at $t = 0.5, 0.75, 1.0, 1.25$ is either 0.120, 0.119, 0.091, or 0.055, which clearly shows that I_0^2 is a very poor candidate for the correct time $t = 1$. On the other hand, Figure 2 shows that the temporal maximum of the function $K_1^2(x, (0.5, 0); t, 1)$ at $t = 0.5, 0.75, 1.0, 1.25$ is either 0.027, 0.026, 0.031, or 0.002, indicating that I_1^2 achieves its maximum at the desired time $t = 1$ and hence yields a much better temporal sensitivity. Therefore, the above numerical comparisons demonstrate that I_1^2 is a better candidate for tracing the moving inhomogeneous inclusion $\cup_{t \in [0, T]} (D(t), t)$. These numerical observations are justified theoretically in sections 3.6 and 3.7.

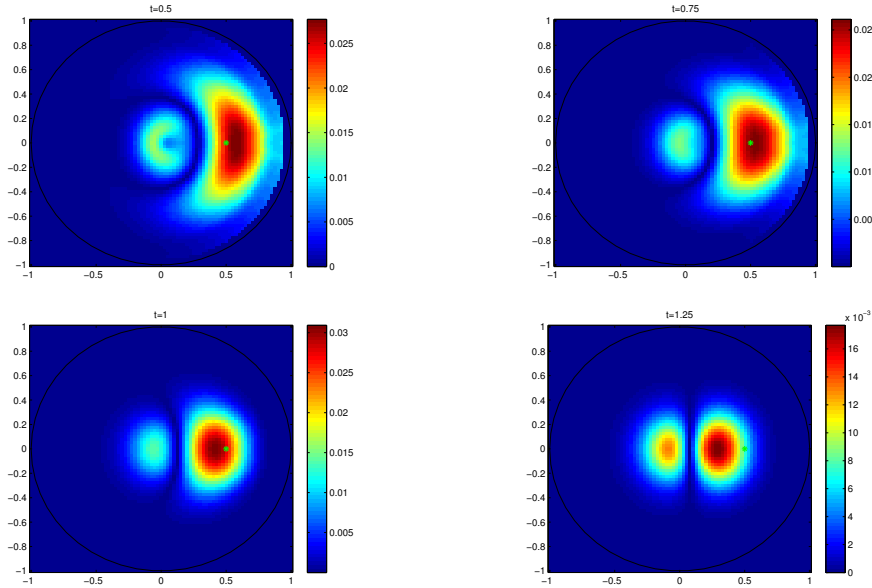


FIG. 2. $I_\gamma^\alpha(\cdot, t)$ for $t = 0.5, 0.75, 1.0, 1.25$, $\alpha = 2, \gamma = 1$, with the scattered field by a point potential $q = \delta_{(0.5,0)}(x)\delta_1(t)$ at the point $(0.5, 0)$ marked by a green star. The maximum in each graph is either 0.027, 0.026, 0.031, or 0.002. Color is available online only.

We can generalize the above construction and define a family of index functions I_γ^α by taking temporal derivatives of I_0^α up to the order γ , i.e.,

$$(3.7) \quad I_\gamma^\alpha = \left(\frac{\partial}{\partial t}\right)^\gamma I_0^\alpha,$$

and its normalized index:

$$(3.8) \quad \hat{I}_\gamma^\alpha(x, t) = \frac{|I_\gamma^\alpha(x, t)|}{\max_{x \in \Omega} |I_\gamma^\alpha(x, t)|}.$$

We shall describe an algorithm for computing this new family of index functions \hat{I}_γ^α in the next subsection and develop in sections 3.6 and 3.7 mathematical justifications of the indices I_γ^α for more accurately locating the time-dependent inhomogeneities inside a homogeneous background. Based on the justifications, we may write, similarly to the approximation (2.7),

$$(3.9) \quad I_\gamma^\alpha(x, t) \approx \sum_{k,j} c_{kj} K_\gamma^\alpha(x, y_k; t, s_j),$$

where $\{(y_k, s_j)\}$ is a set of discrete points in inhomogeneous inclusion $\cup_{t \in (0, T)} (D(t), t)$ and assumed to be sparsely distributed. Then it follows from (3.8) that

$$(3.10) \quad \hat{I}_\gamma^\alpha(x, t) \approx \frac{\sum_{k,j} c_{kj} K_\gamma^\alpha(x, y_k; t, s_j)}{\max_{x \in \Omega} |\sum_{k,j} c_{kj} K_\gamma^\alpha(x, y_k; t, s_j)|}.$$

As will be seen from the asymptotic analysis in sections 3.6 and 3.7, for a sampling point (x, t) that is close to some point (y_l, s_i) , the value of $K_\gamma^\alpha(x, y_k; t, s_j)$ is relatively

large in magnitude for $(k, j) = (l, i)$ and relatively small for $(k, j) \neq (l, i)$, and hence $\hat{I}_\gamma^\alpha(x, t)$ is relatively large. On the other hand, for a sampling point (x, t) that is not close to any point (y_l, s_i) , the value of $K_\gamma^\alpha(x, y_k; t, s_j)$ is small for all (y_k, s_j) , and therefore $\hat{I}_\gamma^\alpha(x, t)$ is also small.

Moreover, the sharpness and the accuracy of the index function $\hat{I}_\gamma^\alpha(x, t)$ are determined by the sharpness of the peak $K_\gamma^\alpha(x, y, t, s)$ and the deviation of the peak maximum at (x, t) from the point (y, s) . Based on our previous numerical comparison between K_1^2 and K_0^2 right after Figure 2, which is also theoretically analyzed in sections 3.6 and 3.7, we conclude that \hat{I}_1^2 provides a better estimate than \hat{I}_0^2 for the location of the inhomogeneous inclusion $\cup_{t \in (0, T)}(D(t), t)$.

3.5. The algorithm. In order to proceed, let us assume, for a given Γ , the following BACKWARD difference approximation rule for a general function $H(t)$ over some mesh points $\{t_j\}_{j=0}^n$ (where $t_n = t$, $t_j - t_{j-1} = h$, and h is a mesh size):

$$\left(\frac{\partial}{\partial t}\right)^\gamma H(t) \approx \frac{1}{h^\gamma} \sum_j A_j^\gamma H(t_{n-j});$$

e.g., if $\gamma = 1$, a legitimate choice will be

$$\left(\frac{\partial}{\partial t}\right) H(t) \approx \frac{1}{h}(H(t) - H(t - h)),$$

and if $\gamma = 2$, one might choose instead

$$\left(\frac{\partial}{\partial t}\right)^2 H(t) \approx \frac{1}{h^2}(H(t) - 2H(t - h) + H(t - 2h)).$$

Let us also choose a quadrature rule over Γ for an integration of a function H defined over Γ as

$$\int_\Gamma H(y) d\sigma_y \approx \sum_\ell b_\ell H(y_\ell).$$

A convenient and stable choice would be a rectangular rule. Given one measurement event, with this choice of Γ , time mesh h , finite difference approximation, and quadrature rule in hand, we are now ready to state the algorithm clearly for computing I_γ^α .

Algorithm I

1. Choose a value of α and δ .
2. For $t = t_a \in [0, T]$, $a = 1, 2, \dots$,
 - For $x = x_b \in \Omega$, $b = 1, 2, \dots$,
 - (a) Obtain measurements $u(x_i, s_j)$ where $x_i \in \Gamma$, $0 < s_j < t_a - \delta$.
 - (b) Compute the value of $I_0^\alpha(x_b, t_a)$ approximately as

$$I_0^\alpha(x_b, t_a) = \frac{\sum_{s_j < t_a - \delta} \sum_i h b_i \eta_{x_b, t_a}^\alpha(x_i, s_j)(f - f_0)(x_i, s_j)}{\sqrt{\sum_{s_j < t_a - \delta} \sum_i h b_i |\eta_{x_b, t_a}^\alpha(x_i, s_j)|^2}}.$$

- For $x = x_b \in \Omega$, $b = 1, 2, \dots$, compute

$$\hat{I}_0^\alpha(x_b, t_a) = \frac{|I_0^\alpha(x_b, t_a)|}{\max_b |I_0^\alpha(x_b, t_a)|}.$$

- For $x = x_b \in \Omega$, $b = 1, 2, \dots$, compute the value of $I_\gamma^\alpha(x_b, t_a)$ approximately as

$$I_\gamma^\alpha(x_b, t_a) = \frac{1}{h^\gamma} \sum_j A_j^\gamma \hat{I}_0^\alpha(x_b, t_{a-j}).$$

- For $x = x_b \in \Omega$, $b = 1, 2, \dots$, compute

$$\hat{I}_\gamma^\alpha(x_b, t_a) = \frac{|I_\gamma^\alpha(x_b, t_a)|}{\max_b |I_\gamma^\alpha(x_b, t_a)|}.$$

3.6. Verification of the index function. In this subsection, we would like to provide a mathematical verification of our newly developed family of index functions I_γ^α . In order to do so, we shall focus on the kernel K_0^α as K_0 defined in (2.5), and their time derivatives K_γ^α as $\partial_t^\gamma K_0^\alpha$, and illustrate that these families of kernels attain their maximum magnitude near $(x, t) = (y, s)$ and decay when (x, t) moves away from (y, s) .

For this purpose, we consider the kernel K_0^α as K_0 defined in (2.5),

$$K_0^\alpha(x, y, t, s) = \frac{\int_0^{\min\{t-\delta, s\}} \int_\Gamma \Phi(y-z, s-k) \Delta_z^\alpha \Phi(x-z, t-k) d\sigma_z dk}{\sqrt{\int_0^{t-\delta} \int_\Gamma (\Delta_z^\alpha \Phi(x-z, t-k))^2 d\sigma_z dk}},$$

and its temporal derivatives:

$$K_\gamma^\alpha(x, y, t, s) := \partial_t^\gamma K_0^\alpha(x, y, t, s).$$

We can readily calculate that

$$(3.11) \quad \Delta_z^\alpha \Phi(x-z, t-k) = \chi_{t>k}(t-k) \frac{1}{4\pi a(t-k)} \exp\left(-\frac{|x-z|^2}{4a(t-k)}\right) \left\{ \frac{|x-z|^{2\alpha}}{4^\alpha a^{2\alpha} (t-k)^{2\alpha}} + O((t-k)^{2\alpha-1}) \right\}.$$

From this, we directly get that there exists a large $t_0 > 0$ such that, for all $t > t_0$,

$$(3.12) \quad \partial_t \left(\sqrt{\int_0^{T-\delta} \int_\Gamma (\Delta_z^\alpha \Phi(x-z, t-k))^2 d\sigma_z dk} \right) = O(t_0^{-2\alpha-2}).$$

This provides us the following explicit expression of K_γ^α for all $\alpha, \gamma \in \mathbb{N}$:

$$(3.13) \quad K_\gamma^\alpha(x, y, t, s) = \frac{\partial_t^\gamma \left(\int_0^{\min\{t-\delta, s\}} \int_\Gamma \Phi(y-z, s-k) \Delta_z^\alpha \Phi(x-z, t-k) d\sigma_z dk \right)}{\sqrt{\int_0^{t-\delta} \int_\Gamma (\Delta_z^\alpha \Phi(x-z, t-k))^2 d\sigma_z dk}} + O(t_0^{-2\alpha-2}).$$

Considering the numerator above, we may directly calculate the temporal derivative for a fixed pair x, y in Ω :

$$\begin{aligned} & \partial_t \left(\int_0^{\min\{t-\delta, s\}} \int_\Gamma \Phi(y-z, s-k) \Delta_z^\alpha \Phi(x-z, t-k) d\sigma_z dk \right) \\ &= \begin{cases} \int_0^{t-\delta} \int_\Gamma \Phi(y-z, s-k) \partial_t \Delta_z^\alpha \Phi(x-z, t-k) d\sigma_z dk - \int_\Gamma \Phi(y-z, s-t+\delta) \Delta_z^\alpha \Phi(x-z, \delta) d\sigma_z & \text{for } t-\delta < s, \\ \int_0^s \int_\Gamma \Phi(y-z, s-k) \partial_t \Delta_z^\alpha \Phi(x-z, t-k) d\sigma_z dk & \text{for } t-\delta > s, \end{cases} \\ &= \begin{cases} -\int_0^{t-\delta} \int_\Gamma \partial_t \Phi(y-z, s-k) \Delta_z^\alpha \Phi(x-z, t-k) d\sigma_z dk + \int_\Gamma \Phi(y-z, s) \Delta_z^\alpha \Phi(x-z, t) d\sigma_z & \text{for } t-\delta < s, \\ -\int_0^s \int_\Gamma \partial_t \Phi(y-z, s-k) \Delta_z^\alpha \Phi(x-z, t-k) d\sigma_z dk \\ \quad + \int_\Gamma \Phi(y-z, s) \Delta_z^\alpha \Phi(x-z, t) d\sigma_z - \int_\Gamma \Phi(y-z, 0) \Delta_z^\alpha \Phi(x-z, t-s) d\sigma_z & \text{for } t-\delta > s, \end{cases} \\ &= \begin{cases} -\int_0^{t-\delta} \int_\Gamma \Delta_z \Phi(y-z, s-k) \Delta_z^\alpha \Phi(x-z, t-k) d\sigma_z dk + \int_\Gamma \Phi(y-z, s) \Delta_z^\alpha \Phi(x-z, t) d\sigma_z & \text{for } t-\delta < s, \\ -\int_0^s \int_\Gamma \Delta_z \Phi(y-z, s-k) \Delta_z^\alpha \Phi(x-z, t-k) d\sigma_z dk + \int_\Gamma \Phi(y-z, s) \Delta_z^\alpha \Phi(x-z, t) d\sigma_z & \text{for } t-\delta > s. \end{cases} \end{aligned}$$

Hence we have for both cases

$$\begin{aligned} & \partial_t \left(\int_0^{\min\{t-\delta, s\}} \int_{\Gamma} \Phi(y-z, s-k) \Delta_z^\alpha \Phi(x-z, t-k) d\sigma_z dk \right) \\ &= - \int_0^{\min\{t-\delta, s\}} \int_{\Gamma} \Delta_z \Phi(y-z, s-k) \Delta_z^\alpha \Phi(x-z, t-k) d\sigma_z dk + \int_{\Gamma} \Phi(y-z, s) \Delta_z^\alpha \Phi(x-z, t) d\sigma_z. \end{aligned}$$

This, along with the fact that, for all $s, t > t_0$,

$$\int_{\Gamma} \Phi(y-z, s) \Delta_z^\alpha \Phi(x-z, t) d\sigma_z = O(t_0^{-2\alpha-2})$$

enables us to derive an explicit expression for the kernel $K_\gamma^\alpha(x, y; t, s)$ for all the testing points $(x, t), (y, s)$ from $\Omega \times (t_0, T)$:

(3.14)

$$K_\gamma^\alpha(x, y; t, s) = \frac{-\partial_t^{\gamma-1} \left(\int_0^{\min\{t-\delta, s\}} \int_{\Gamma} \Delta_z \Phi(y-z, s-k) \Delta_z^\alpha \Phi(x-z, t-k) d\sigma_z dk \right)}{\sqrt{\int_0^{T-\delta} \int_{\Gamma} (\Delta_z^\alpha \Phi(x-z, t-k))^2 d\sigma_z dk}} + O(t_0^{-2\alpha-2}).$$

Inductively, we can use the same argument as above to calculate the γ th derivative for the denominator in (3.13); then we come to the following approximation for all test points $(x, t), (y, s)$ from $\Omega \times (t_0, T)$:

(3.15)

$$K_\gamma^\alpha(x, y; t, s) = (-1)^\gamma \frac{\int_0^{\min\{t-\delta, s\}} \int_{\Gamma} \Delta_z^\gamma \Phi(y-z, s-k) \Delta_z^\alpha \Phi(x-z, t-k) d\sigma_z dk}{\sqrt{\int_0^{T-\delta} \int_{\Gamma} (\Delta_z^\alpha \Phi(x-z, t-k))^2 d\sigma_z dk}} + O(t_0^{-2\alpha-2}).$$

This approximation implies for all x, y such that $d(x, \partial\Omega) > \varepsilon, d(y, \partial\Omega) > \varepsilon$ for some $\varepsilon > 0$ that

(3.16)

$$\begin{aligned} K_\gamma^\alpha(x, y; t, s) &= (-1)^\gamma \frac{\int_0^{\min\{t-\delta, s-\delta\}} \int_{\Gamma} \Delta_z^\gamma \Phi(y-z, s-k) \Delta_z^\alpha \Phi(x-z, t-k) d\sigma_z dk}{\sqrt{\int_0^{T-\delta} \int_{\Gamma} (\Delta_z^\alpha \Phi(x-z, t-k))^2 d\sigma_z dk}} + O(t_0^{-2\alpha-2}) + O(\delta) \\ &= (-1)^\gamma \frac{\langle \eta_{y,s}^\gamma, \eta_{x,t}^\alpha \rangle_{L^2((0,T) \times \Gamma)}}{|\eta_{x,t}^\alpha|_{L^2((0,T) \times \Gamma)}} + O(t_0^{-2\alpha-2}) + O(\delta). \end{aligned}$$

One can now see from the expression (3.16) for $\gamma = \alpha$ that the kernel K_α^α attains its maximum magnitude when $x \approx y$ and $t \approx s$ and is small otherwise.

Next, we consider the case with $\gamma < \alpha$. Using the fact that

$$\Delta_z^\gamma \Phi(y-z, s-k) = \Delta_z^\gamma \Phi(y-z, s-k)$$

and the expression (3.14), we know that the kernel K_γ^α satisfies

$$(3.17) \quad (-\Delta_y)^{(\alpha-\gamma)} K_\gamma^\alpha(x, y, t, s) = K_\alpha^\alpha(x, y, t, s) + O(t_0^{-2\alpha-2}).$$

Now we write L_y as the following volume integral operator in the ball $B_R(0)$ of a radius R , i.e.,

$$(3.18) \quad [L_y f](y) = -\frac{1}{2\pi} \int_{B_R(0)} \log(|p-y|) f(p) dp = -\frac{1}{2\pi} [\log(|\cdot|) * f](y)$$

for all $y \in B_R(0)$, as well as the following two boundary integral operators on $\partial B_R(0)$:

$$(3.19) \quad [S_y F](y) = \frac{1}{2\pi} \int_{\partial B_R(0)} \log(|y - p|) \partial_n F(p) d\sigma_p$$

and

$$(3.20) \quad [D_y F](y) = -\frac{1}{2\pi} \int_{\partial B_R(0)} \partial_n \log(|y - p|) F(p) d\sigma_p$$

for $y \in B_R(0)$. With these notations at hand, we can directly get from (3.17) and the Green's identity that, for all $\gamma < \alpha$,

$$(3.21) \quad K_{\alpha-1}^\alpha(x, y; t, s) = [L_y K_\alpha^\alpha](x, y, t, s) + [S_y K_{\alpha-1}^\alpha](x, y, t, s) + [D_y K_{\alpha-1}^\alpha](x, y, t, s) + O(t_0^{-2\alpha-2}).$$

But, from (3.11), we can directly get that, as y goes to infinity, for all $\gamma, m \in \mathbb{N}$,

$$(3.22) \quad \Delta_y^\gamma \Phi(y - z, s - k) = O(|y|^{-m});$$

therefore, as y goes to infinity, we get that for all $\alpha, m \in \mathbb{N}$,

$$(3.23) \quad K_\gamma^\alpha(x, y, t, s) = O(|y|^{-m}).$$

From this, together with (3.21), we deduce that for all $m \in \mathbb{N}$,

$$(3.24) \quad K_{\alpha-1}^\alpha(x, y; t, s) = [L_y K_\alpha^\alpha](x, y, t, s) + O(t_0^{-2\alpha-2}) + O(R^{-m}).$$

With the same arguments, we can inductively get that for all $\gamma < \alpha$,

$$(3.25) \quad K_\gamma^\alpha(x, y; t, s) = [L_y^{(\alpha-\gamma)} K_\alpha^\alpha](x, y, t, s) + O(t_0^{-2\alpha-2}) + O(R^{-m}).$$

Recall from (3.16) that K_α^α attains its maximum magnitude when $x \approx y$ and $t \approx s$ and is small otherwise. On the other hand, we see from (3.25) that $K_\gamma^\alpha(x, y, t, s)$ has its maximum near $x \approx y$ and $t \approx s$ for $\gamma \leq \alpha$. However, due to the diffusive nature of the kernel of the volume integral operator L_y , a successive application of the operator (i.e., $(\alpha - \gamma)$ increases) will make the kernel K_γ^α become less and less sharp, and the maximum may be located further and further away from the set $\{x = y, t = s\}$. This behavior of the kernel K_γ^α , together with (2.7), indicates that the support of our index function provides a reasonable estimate of the locations of inhomogeneities as soon as $(\alpha - \gamma)$ is small. This also provides a theoretical explanation of why the kernel K_1^2 (Figure 2) behaves better than K_0^2 (Figure 1).

3.7. More detailed behaviors of the index functions. From the previous subsection, we have shown that the index function K_γ^α attains its maximum around $x \approx y$ and $t \approx s$ for $\gamma \leq \alpha$.

Theoretically speaking, from the previous subsection, we can conclude that the kernel behaves the best when $\gamma = \alpha$ and is less sharp when $\gamma < \alpha$. However, in practice, a higher value of γ implies a higher order of numerical derivatives, which is less stable and less robust with the presence of noise. Therefore, in practice, it is undesirable to have a very large value of γ . As we observed numerically in sections 3.3 and 3.4, the index function $\hat{I}_\gamma^\alpha(x, t)$ works well enough for $\alpha = 2$ and $\gamma = 1$. It is chosen as a balance of the theoretical sharpness of the kernel and the numerical robustness against noise when numerical derivatives are taken.

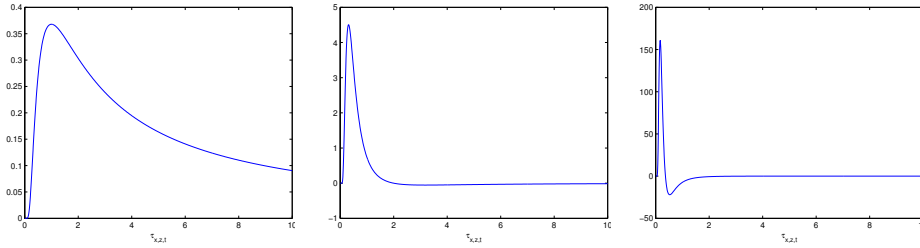


FIG. 3. The graphs of g_1 , g_2 , and g_3 against the variable $\tau_{x,z,t}$ for a fixed value of $|x - z|$.

So, in this section, we would like to focus on this special case and study the behavior of these kernels and how far the maximum of the kernels might deviate from the set $\{x = y, t = s\}$.

We shall now examine the cases with $\alpha = 2$ and $\gamma = 0, 1$, i.e., the kernels $K_0^2(x, y, t, s)$ and $K_1^2(x, y, t, s) := \partial_t K_0^2(x, y, t, s)$. For this purpose, we can calculate explicitly as follows:

$$\begin{aligned} \Phi(x - z, t - k) &= \chi_{t > k}(t - k) \frac{1}{4\pi a(t - k)} \exp\left(-\frac{|x - z|^2}{4a(t - k)}\right), \\ \nabla_z \Phi(x - z, t - k) &= \chi_{t > k}(t - k) \frac{1}{4\pi a(t - k)} \exp\left(-\frac{|x - z|^2}{4a(t - k)}\right) \frac{1(x - z)}{2a(t - k)}, \\ \Delta_z \Phi(x - z, t - k) &= \chi_{t > k}(t - k) \frac{1}{4\pi a(t - k)} \exp\left(-\frac{|x - z|^2}{4a(t - k)}\right) \left(\frac{|x - z|^2}{4a^2(t - k)^2} - \frac{1}{2a(t - k)}\right) \end{aligned}$$

and

$$\begin{aligned} \Delta_z^2 \Phi(x - z, t - k) &= \chi_{t > k}(t - k) \frac{1}{4\pi a(t - k)} \exp\left(-\frac{|x - z|^2}{4a(t - k)}\right) \left\{ \left(\frac{|x - z|^2}{4a^2(t - k)^2} - \frac{1}{2a(t - k)}\right)^2 - \frac{|x - z|^2}{2a^3(t - k)^3} + \frac{1}{2a^2(t - k)^2} \right\} \\ &= \chi_{t > k}(t - k) \frac{1}{4\pi a(t - k)} \exp\left(-\frac{|x - z|^2}{4a(t - k)}\right) \left\{ \frac{|x - z|^4}{16a^4(t - k)^4} - \frac{3|x - z|^2}{4a^3(t - k)^3} + \frac{3}{4a^2(t - k)^2} \right\}. \end{aligned}$$

We now introduce another variable to simplify the notation. For a fixed pair x, z , we shall rewrite the fundamental solution and its derivatives using the variable $\tau_{x,z,t} = \frac{4a(t-k)}{|x-z|^2}$ as

$$\begin{aligned} \Phi(x - z, t - k) &= |x - z|^{-2} g_1(\tau_{x,z,t}) := \chi_{t < k}(\tau_{x,z,t}) |x - z|^{-2} \exp\left(-\tau_{x,z,t}^{-1}\right) \tau_{x,z,t}^{-1}, \\ \Delta_z \Phi(x - z, t - k) &= |x - z|^{-4} g_2(\tau_{x,z,t}) := \chi_{t < k}(\tau_{x,z,t}) |x - z|^{-4} \exp\left(-\tau_{x,z,t}^{-1}\right) \left\{ \frac{4}{\tau_{x,z,t}^3} - \frac{2}{\tau_{x,z,t}^2} \right\}, \\ \Delta_z^2 \Phi(x - z, t - k) &= |x - z|^{-6} g_3(\tau_{x,z,t}) := \chi_{t < k}(\tau_{x,z,t}) |x - z|^{-6} \exp\left(-\tau_{x,z,t}^{-1}\right) \left\{ \frac{16}{\tau_{x,z,t}^5} - \frac{48}{\tau_{x,z,t}^4} + \frac{12}{\tau_{x,z,t}^3} \right\}. \end{aligned}$$

From these expressions, we can see the clear asymptotic behavior for the functions with fixed x, z, t as $\tau_{x,z,t}$ goes to 0 or ∞ . In Figure 3, we have plotted the three functions g_1, g_2 , and g_3 above, from which we can see that the peaks of g_i grow sharper as i increases, and their peak is attained at either $\tau_{x,z,t} = 1$, $\tau_{x,z,t} = \frac{7-\sqrt{33}}{4} \approx 0.3139$, or

$$\tau_{x,z,t} = \frac{17}{9} - \frac{\sqrt{579}}{9} \sin \frac{\tan^{-1} \frac{6\sqrt{7998}}{2627}}{3} - \frac{\sqrt{193}}{9} \cos \frac{\tan^{-1} \frac{6\sqrt{7998}}{2627}}{3} \approx 0.1693.$$

With the help of these notions, we can directly compute that

$$\begin{aligned} \int_0^{\min\{t-\delta,s\}} \int_{\Gamma} \Phi(y-z, s-k) \Delta_z^2 \Phi(x-z, t-k) d\sigma_z dk &= \int_{\Gamma} \int_0^{\min\{t-\delta,s\}} \frac{g_1(\tau_{y,z,s}) g_3(\tau_{x,z,t}) dk}{|y-z|^2 |x-z|^6} d\sigma_z, \\ \int_0^{\min\{t-\delta,s\}} \int_{\Gamma} \Delta_z \Phi(y-z, s-k) \Delta_z^2 \Phi(x-z, t-k) d\sigma_z dk &= \int_{\Gamma} \int_0^{\min\{t-\delta,s\}} \frac{g_2(\tau_{y,z,s}) g_3(\tau_{x,z,t}) dk}{|y-z|^4 |x-z|^6} d\sigma_z, \\ \int_0^{t-\delta} \int_{\Gamma} (\Delta_z^2 \Phi(x-z, t-k))^2 d\sigma_z dk &= \int_0^{t-\delta} \int_{\Gamma} |x-z|^{-12} |g_3(\tau_{x,z,t})|^2 d\sigma_z dk. \end{aligned}$$

Then a change of variables for the integrant gives

$$\begin{aligned} &\int_0^{\min\{t-\delta,s\}} \int_{\Gamma} \Phi(y-z, s-k) \Delta_z^2 \Phi(x-z, t-k) d\sigma_z dk \\ &= \int_{\Gamma} |y-z|^{-2} |x-z|^{-4} \left(\int_0^{\frac{4a(t-\delta)}{|x-z|^2}} g_1 \left(\frac{|x-z|^2}{|y-z|^2} \tau - \frac{4a(t-s)}{|y-z|^2} \right) g_3(\tau) d\tau \right) d\sigma_z, \end{aligned} \tag{3.26}$$

$$\begin{aligned} &\int_0^{\min\{t-\delta,s\}} \int_{\Gamma} \Delta_z \Phi(y-z, s-k) \Delta_z^2 \Phi(x-z, t-k) d\sigma_z dk \\ &= \int_{\Gamma} |y-z|^{-4} |x-z|^{-4} \left(\int_0^{\frac{4a(t-\delta)}{|x-z|^2}} g_2 \left(\frac{|x-z|^2}{|y-z|^2} \tau - \frac{4a(t-s)}{|y-z|^2} \right) g_3(\tau) d\tau \right) d\sigma_z, \end{aligned} \tag{3.27}$$

$$\begin{aligned} &\int_0^{\frac{4a(t-\delta)}{|x-z|^2}} (\Delta_z^2 \Phi(x-z, t-k))^2 d\sigma_z dk \\ &= \frac{1}{4a} \int_{\Gamma} |x-z|^{-10} \int_0^{\frac{4a(t-\delta)}{|x-z|^2}} |g_3(\tau)|^2 d\tau d\sigma_z, \end{aligned} \tag{3.28}$$

where it holds for $t > t_0$ that

$$\int_0^{t-\delta} \int_{\Gamma} (\Delta_z^2 \Phi(x-z, t-k))^2 d\sigma_z dk = \frac{1}{4a} \int_{\Gamma} |x-z|^{-10} \int_0^{\infty} |g_3(\tau)|^2 d\tau d\sigma_z + O(t_0^{-6})$$

or

$$C_1(t_0) \int_{\Gamma} |x-z|^{-10} d\sigma_z \leq \int_0^{t-\delta} \int_{\Gamma} (\Delta_z^2 \Phi(x-z, t-k))^2 d\sigma_z dk \leq C_2(t_0) \int_{\Gamma} |x-z|^{-10} d\sigma_z,$$

where the difference $C_1 - C_2$ tends to 0 as $t_0 \rightarrow \infty$. This indicates that the denominator of (3.14) gives only a spatial weighting independent of time.

Now we can directly see from (3.26)–(3.28) that since g_1 's peak is not steep, with a slowly decaying tail, the correlation between the function g_1 and the sharp peaked function g_3 does not give a sharp maximum even when the peaks of g_1 and g_3 coincide. Hence K_0^2 (see (3.14)) does not have a very sharp maximum sitting near the set $\{x = y, t = s\}$. On the other hand, as g_2 's peak is much sharper, the correlation between two very sharp peaked functions g_2 and g_3 provides a much sharper maximum when both peaks of g_2 and g_3 are close. Therefore, the maximum of K_1^2 provides a clearer and sharper peak sitting near the set $\{x = y, t = s\}$.

Next, we would like to focus on a possible time delay for the index functions, i.e., the discrepancy of the maxima of the two indices K_0^2 and K_1^2 at $s = t$. We have

already shown that the maxima of the kernels are near each other but may deviate from the set $\{x = y, t = s\}$.

Let $C_1 > 0$ be given. For any small $\varepsilon > 0$, we now fix x, y in Ω such that $d(x, \Gamma) > \varepsilon$, $d(y, \Gamma) > \varepsilon$, and $|x - y| < C_1\varepsilon^2$; then, for any $z \in \Gamma$, we have

$$\left| \frac{|y - z|}{|x - z|} - 1 \right| \leq \frac{|y - x|}{|x - z|} \leq C_1\varepsilon.$$

From (3.26)–(3.28), we can directly see with this fixed pair of x, y that the correlation between a scaled g_1 and g_3 in the integrand (3.26) attains a maximum when the maxima of functions $g_1\left(\frac{|x-z|^2}{|y-z|^2}(\cdot) - \frac{4a(t-s)}{|y-z|^2}\right)$ and $g_3(\cdot)$ coincide, i.e., when

$$\frac{4a(t-s)}{|y-z|^2} = 1 \times \frac{|y-z|^2}{|x-z|^2} - 0.1693 < 0.8307 + 3 \max\{C_1, C_2^2\}\varepsilon,$$

with $C_2 = \text{diam}(\Omega)^2$. Therefore, the whole integral of (3.26) reaches a maximum when

$$(3.29) \quad t - s < \frac{C_2}{a} (0.8307 + 3 \max\{C_1, C_2^2\}\varepsilon).$$

Similarly, we can see for this fixed pair of x, y that the correlation between a scaled g_2 and g_3 attains the maximum when $g_1\left(\frac{|x-z|^2}{|y-z|^2}(\cdot) - \frac{4a(t-s)}{|y-z|^2}\right)$ and $g_3(\cdot)$ coincide, i.e., when

$$\frac{4a(t-s)}{|y-z|^2} = 0.3139 \times \frac{|y-z|^2}{|x-z|^2} - 0.1693 < 0.1446 + 3 \max\{C_1, C_2^2\}\varepsilon.$$

Therefore, the whole integral (3.27) reaches a maximum when

$$(3.30) \quad t - s < \frac{C_2}{a} (0.1446 + 3 \max\{C_1, C_2^2\}\varepsilon).$$

In summary, we may see from above that, although K_γ^2 in (3.16) attains a maximum when $s \approx t$, $x \approx y$, as was argued in the previous section, there is a possible shift of the maximum for different K_γ^2 . Also, as we know from (3.12) that the value of the denominator is nearly a constant with respect to t for large $t > t_0$, so we do not need to take care of it. Now, for a given source time $s > t_0$, comparing the upper bounds provided by (3.29) and (3.30), we know that the sampling time t that brings K_γ^2 to a maximum is allowed to have a magnitude of delay different from s , and the delay is much more significant in K_0^2 than in K_1^2 .

The above analysis helps us understand the following behaviors of the index functions in terms of their sharpness and time delay: the maximum is much shifted for K_0^2 and not sharp, while the maximum is much less shifted for K_1^2 , close to $s = t$, but it is much sharper.

Similar analysis can be carried out for different α and $\gamma \leq \alpha$ to provide a similar generic conclusion that the maximum is increasingly shifted from $t = s$ and also loses its sharpness as γ decreases from α .

3.8. Alternative characterization of the index functions. In this subsection, we would like to provide an alternative characterization of our newly developed index functions and explain the new DSM in the concept of a forward-projection technique.

Although this new way of understanding does not, for now, bring forth new computational techniques for evaluating our index function, it brings us to a new and deeper understanding of our method, which might possibly suggest further modification of the index function or the extension of our method to a more general case.

For this purpose, we first define an auxiliary function $\psi(x, t)$, which meets the initial condition $\psi(x, 0) = 0$ in Ω and solves the equation

$$\partial_t \psi(x, t) = a \Delta_x \psi(x, t) \quad \text{in } \Omega,$$

with the boundary condition $\partial_n \psi(x, t) = (f - f_0)(x, t)$ for $x \in \Gamma, t \in (0, T)$. Then we readily get

$$(3.31) \quad \psi(x, t) = \int_0^t \int_{\Gamma} (f - f_0)(y, s) G(x, t; y, s) d\sigma_y ds,$$

where $G(x, t; y, s)$ is the Neumann Green's function for the heat equation

$$\partial_t G(x, t; y, s) - a \Delta_x G(x, t; y, s) = \delta_s(t) \delta_y(x) \quad \text{in } \Omega,$$

with the boundary condition $\partial_n G(x, t; y, s) = 0$ for $x \in \Gamma$. Clearly, we can write

$$\partial_t (\Phi(x - y, t - s) - G(x, t; y, s)) - a \Delta_x (\Phi(x - y, t - s) - G(x, t; y, s)) = 0 \quad \text{in } \Omega,$$

with the boundary condition $\partial_n (\Phi(x - y, t - s) - G(x, t; y, s)) = -\partial_n \Phi(x - y, t - s)$ for $x \in \Gamma$. For a fixed $y \in \Omega$, we have for $m \in \mathbb{N}$,

$$-\Phi(x - y, t - s) = O(R^{-m}) \quad \text{as } 2R \geq \text{diam}(\Omega).$$

This implies the estimate

$$\|\Phi(x - y, t - s) - G(x, t; y, s)\|_{L^2((0, T) \times \Gamma)} = O(R^{-m}).$$

Using this, we can write

$$(3.32) \quad \begin{aligned} \psi(x, t) &= \int_0^t \int_{\Gamma} (f - f_0)(y, s) \Phi(x - y, t - s) d\sigma_y ds + O(R^{-m}) \\ &= \int_0^{t-\delta} \int_{\Gamma} (f - f_0)(y, s) \Phi(x - y, t - s) d\sigma_y dt + O(R^{-m}) + O(\delta). \end{aligned}$$

Similarly, we can derive

$$(3.33) \quad \begin{aligned} \Delta_x^\alpha \psi(x, t) &= \int_0^{t-\delta} \int_{\Gamma} (f - f_0)(y, s) \Delta_x^\alpha \Phi(x - y, t - s) d\sigma_z dt + O(R^{-m}) + O(\delta) \\ (3.34) \quad &= \langle \eta_{x,t}^\alpha, f - f_0 \rangle_{L^2((0, T) \times \Gamma)} + O(R^{-m}) + O(\delta). \end{aligned}$$

This observation suggests that we use the auxiliary function ψ for an alternative characterization of the index function I_0^α :

$$(3.35) \quad I_0^\alpha(x, t) = \frac{\Delta_x^\alpha \psi(x, t)}{|\eta_{x,t}^\alpha|_{L^2((0, T) \times \Gamma)}} + O(R^{-m}) + O(\delta).$$

It follows from the same argument as used above that, for all $t > t_0$,

$$(3.36) \quad I_\gamma^\alpha(x, t) = \frac{\partial_t^\gamma \Delta_x^\alpha \psi(x, t)}{|\eta_{x,t}^\alpha|_{L^2((0,T) \times \Gamma)}} + O(R^{-m}) + O(\delta) + O(t_0^{-2\alpha-2}).$$

We notice that the denominator $|\eta_{x,t}^\alpha|_{L^2((0,T) \times \Gamma)}$ may be calculated beforehand. Therefore, the formulas (3.35) and (3.36) provide an efficient alternative mean to compute the index functions when the radius of the domain is large and the cut-off parameter δ is small.

The above characterization of I_γ^α using the auxiliary function ψ may help us illustrate our new DSM as a forward-projection process. To see this, we introduce a linear operator L :

$$(3.37) \quad [L(h)](x, t) = \int_0^t \int_{\mathbb{R}^2} \Phi(x - y, t - s) h(y, s) \, dy ds \quad \text{for all } h \in L^2((0, T) \times \Omega),$$

where Φ is the fundamental solution to the heat equation, and the trace operator $E : H^1(\partial\Omega) \rightarrow L^2(\Gamma)$. Then we can restate (2.2) as

$$(3.38) \quad [E \circ L](c) = f - f_0.$$

Here we would like to remark that, for the recovery of the source c from the scattered field $f - f_0$, the popular back-projection technique or time reversal method is to perform the action of the adjoint $[E \cdot L]^*$ on both sides of the equation after applying a weighting operator W to $f - f_0$:

$$(3.39) \quad [E \circ L]^* W [E \circ L](c) = [E \circ L]^* W (f - f_0) = \int_\tau^T \int_\Gamma \Phi(z - y, s - \tau) [W(f - f_0)](y, s) \, dy ds.$$

Hence the function $\phi := [E \circ L]^* W (f - f_0)$ satisfies a time-reversed heat equation

$$\partial_t \phi = -a \Delta_x \phi \quad \text{in } \Omega,$$

with some appropriate boundary conditions related to $f - f_0$ and a final time condition at $t = T$.

However, the construction of our auxiliary function ψ is quite different. In fact, ψ satisfies a forward heat equation

$$\partial_t \psi = a \Delta_x \psi \quad \text{in } \Omega.$$

Therefore, the linear operator $Q : (f - f_0) \mapsto \psi$ can be regarded as a forward-projection operator, and our indices I_γ^α can be calculated as the spatial-temporal derivatives of the forward projection $Q(f - f_0)$.

4. Stabilization techniques in numerical implementations. In this section, we discuss several numerical strategies and the detailed numerical implementation of the newly developed DSM method.

4.1. Numerical stabilization of the index function. For a stable computation of our time-dependent index function \hat{I}_1^2 , we now consider some postprocessing stabilization steps to improve the location estimates by the index \hat{I}_1^2 . As we have

seen in the previous sections, the sharpness of I_γ^α increases with increasing γ (up to α) while the possible shift of the maximum (i.e., the time delay) decreases. However, increasing γ implies taking more temporal derivatives of the index I_0^α , which is evaluated as an inner product between the measurement data and probing functions. Hence the index I_γ^α becomes more expensive computationally with increasing γ and is also more sensitive to noise in the data numerically. Therefore, we suggest choosing the index I_1^2 (with $\alpha = 2$ and $\gamma = 1$) to balance the computational efficiency and numerical stability.

The following two forms of cut-offs appear to be very helpful for increasing the numerical stability of the index function and improve the reconstruction profile sharply:

(1) As we locate the inclusions by evaluating the index function, which gives large values near the exact inclusion, we choose a threshold C and determine the reconstructed inclusion as the support of the index function according to the threshold.

(2) We notice some instability at the origin, i.e., the center of the domain, from our numerical experiments. This is mainly caused by the very weak signal from the center of the domain. Therefore, we truncate the index value at the center to zero (and only at the center). This is to make a prior assumption that the exact inclusion does not hit the center of the domain. In fact, such an assumption is not too restrictive. It is thanks to the fact that the computation of an index function at a particular time t_0 does not depend on the index function before t_0 or after t_0 . Therefore, even when the assumption is violated at a particular time interval $[t_1, t_2]$, only the frames where the inclusions hit the center during $[t_1, t_2]$ will be affected, and those frames before $t < t_1$ or after $t > t_2$ will not be affected, and the index function will still work.

Next, we apply a temporal mollifier for the index function \hat{I}_γ^α to smoothen any possible sudden jump of the index function due to the numerical instability from the noise. It might happen that at some particular time frame the index function may differ from several previous ones with the presence of noise, and then, after that particular frame, it will come back to its previous position. To stabilize, the following simple linear mollifier with a kernel g under some numerical quadrature rule,

$$(4.1) \quad \tilde{I}_\gamma^\alpha(\cdot, t) = \int_0^t \hat{I}_\gamma^\alpha(\cdot, s)g(s)ds \approx \sum_i a_i \hat{I}_\gamma^\alpha(\cdot, t - h_i),$$

is a natural choice, but this does not work very well because this linear mollification does not add any credit to the support of $\tilde{I}_\gamma^\alpha(\cdot, t)$ that is stable over time. Our aim is to sort out the path of motion for the inclusion which moves stably over time. Therefore, we should seek a mollification process which credits this stability over time and magnifies a value of the function $\tilde{I}_\gamma^\alpha(\cdot, t)$ at a point x when the previous values of $\tilde{I}_\gamma^\alpha(x, s)$ are large for $t - \delta_t < s < t$ for some δ_t . This property of the mollification process that we hope to acquire reflects the fact that, when the location is marked by a large value for a period of time $(t - \delta_t, t)$, this location should be more likely to give a better estimate of the location of inhomogeneity. A technique for actualizing such a property is also called a fading-memory technique, where the previous “memories” are used together with existing received signals to determine the current reconstruction. In our numerical implementation, we notice that the following nonlinear mollification process provides such an aforementioned advantage:

$$(4.2) \quad \tilde{I}_\gamma^\alpha(\cdot, t) = a_0 \prod_i \chi_{\text{supp}(I_\gamma^\alpha(\cdot, t-h_i))} \hat{I}_\gamma^\alpha(\cdot, t) + \left(1 - \prod_i \chi_{\text{supp}(\hat{I}_\gamma^\alpha(\cdot, t-h_i))} I_\gamma^\alpha(\cdot, t) \right) \sum_i a_i \hat{I}_\gamma^\alpha(\cdot, t - h_i),$$

where we always choose all weights $a_i = 0$, except that $a_0 = 0.75$ and $a_i = 0.05$ for $i = 1, 2, \dots, 5$. The effect of this mollification is that it only favors a maximum value that stays there for five consecutive frames. Then we normalize this mollified new index as before:

$$(4.3) \quad \hat{I}_\gamma^\alpha(x, t) = \frac{|\hat{I}_\gamma^\alpha(x, t)|}{\max_{x \in \Omega} |\hat{I}_\gamma^\alpha(x, t)|}.$$

This mollification strategy takes into account the information from the previous time frames, so it can greatly stabilize the numerical reconstructions over the time and provide a reasonable estimate of the inhomogeneous inclusions at the correct time.

To be more precise, we formulate an algorithm for computing the index \hat{I}_γ^α .

Algorithm II

1. Choose $\alpha, \gamma \in \{0, 1, 2\}$, small $\delta > 0$; set $a_0 = 0.75$, $a_i = 0.05$ for $i = 1, \dots, 5$ and $a_i = 0$ for $i > 5$.
2. For $t = t_a \in [0, T]$, $a = 1, 2, \dots, n$,
 - Obtain measurements $u(x_i, s_j)$ where $x_i \in \Gamma$, $0 < s_j < t_a - \delta$.
 - For each sampling point $x_b \in \Omega$, $b = 1, 2, \dots$, compute $\hat{I}_\gamma^\alpha(x_b, t_a)$ by **Algorithm I**.
3. For $t = t_a \in [0, T]$, $a = 1, 2, \dots, n$,
 - For each sampling point $x_b \in \Omega$, $b = 1, 2, \dots$, compute

$$\begin{aligned} \tilde{I}_\gamma^\alpha(x_b, t_a) &= a_0 \prod_i \chi_{\text{supp}(I_\gamma^\alpha(\cdot, t_a - h_i))} \hat{I}_\gamma^\alpha(x_b, t_a) \\ &\quad + \left\{ 1 - \prod_i \chi_{\text{supp}(\hat{I}_\gamma^\alpha(\cdot, t_a - h_i))} I_\gamma^\alpha(x_b, t_a) \right\} \sum_i a_i \hat{I}_\gamma^\alpha(x_b, t_a - h_i). \end{aligned}$$

- For each sampling point $x_b \in \Omega$, $b = 1, 2, \dots$, compute

$$\hat{I}_\gamma^\alpha(x_b, t_a) = \frac{|\hat{I}_\gamma^\alpha(x_b, t_a)|}{\max_{x \in \Omega} |\hat{I}_\gamma^\alpha(x, t_a)|}.$$

Figure 4 shows the value of the kernel $\hat{I}_1^2(\cdot, t)$ at $t = 0.5, 0.75, 1.0, 1.25$ coming from a point potential $q = \delta_{(0.5, 0)}(x)\delta_1(t)$. From the plots in Figure 4, we can see that, after the stabilization process and thresholds, the index function provides a very sharp maximum attained very close to $x = (0.5, 0)$ at $t = 1$ and an accurate estimate of the location of the space-time inclusion.

4.2. Locating inhomogeneities from index functions and stabilization processes. We now discuss the issue of locating inhomogeneous inclusions from the index functions and establish some further stabilization techniques.

The reconstruction of the inhomogeneities can be done practically by a greedy search algorithm for possible clusters of I_γ^α , and then the location of the inhomogeneity corresponding to each cluster can be pinpointed by calculating the corresponding centers of mass for each cluster from the values of the index function. The trajectory of each reconstructed inclusion $\Gamma^{\text{recon}}(t)$ is then given by the center of mass of each cluster at a different time t .

As we have already noticed in subsection 3.6, our verifications (3.16)–(3.25) indicate that the index is accurate only for $t > t_0$ with large t_0 .

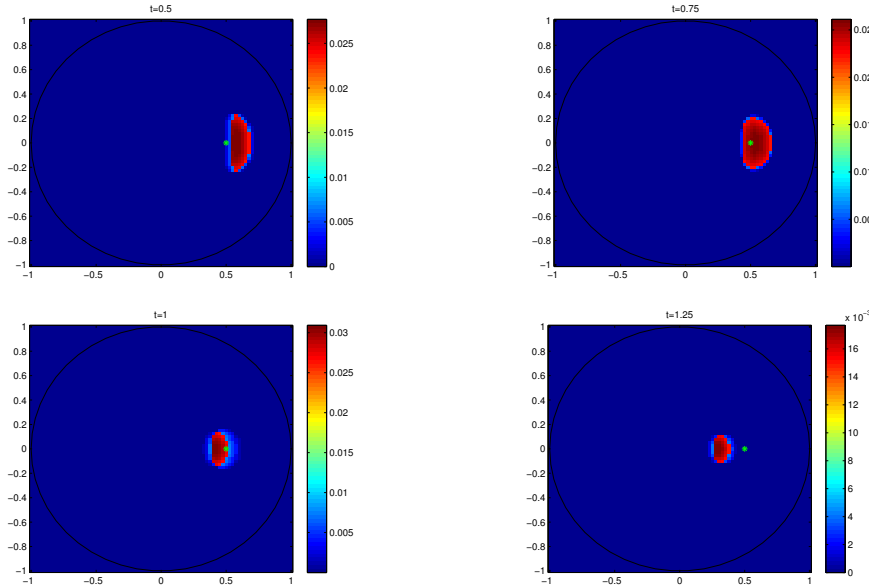


FIG. 4. $\hat{I}_\gamma^\alpha(\cdot, t)$ for $t = 0.5, 0.75, 1.0, 1.25$, $\alpha = 2, \gamma = 1$, with the scattered field by a point potential $q = \delta_{(0.5,0)}(x)\delta_1(t)$, with $(0.5, 0)$ marked by a green star. Color is available online only.

Indeed, this observation that the index is not accurate for $t < t_0$ can be explained physically by the fact that the diffusion equation is forward-propagating and we do not have information of the heat distribution before $t < 0$ to give sufficient information altogether for the location of the inclusions for $t < t_0$.

The formula (3.16)–(3.25) tells us that the error decays quickly with the order $O(t_0^{-2\alpha-2})$. With such an error order in (3.16)–(3.25), the error can be practically small enough with a constant t_0 just slightly larger than 1. Therefore, it is numerically practical to consider only I_γ^α for $t > t_0$ with a threshold t_0 which may need not be too large. From our numerical experiments, we usually notice that the index for $t < 0.5$ is quite unstable and deviates from the exact trajectory. With this observation, we shall make a prior assumption that we know the initial positions (and only the initial positions) of the inclusions and define a prior-corrected trajectory as

$$(4.4) \quad \Gamma_{\text{prior}}^{\text{recon}}(t) := (1 - \exp(-\lambda^2 t^2)) \Gamma^{\text{recon}}(t) + \exp(-\lambda^2 t^2) \Gamma^{\text{exact}}(0),$$

where λ is a constant which is selected to be not too small so that the exact initial location $\Gamma^{\text{exact}}(0)$ does not dominate the estimate $\Gamma_{\text{prior}}^{\text{recon}}(t)$. We shall take λ in the range $1/2 < \lambda < 2$.

In order to enhance numerical stability, after acquiring the trajectory of the reconstructed inclusion $\Gamma_{\text{prior}}^{\text{recon}}(t)$, we further perform an H^1 -regularization of the trajectory, i.e., minimizing the functional

$$(4.5) \quad J(\Gamma) := \frac{1}{2} \|\Gamma - \Gamma_{\text{prior}}^{\text{recon}}\|_{L^2((0,t))}^2 + \frac{\beta}{2} \|\partial_s \Gamma\|_{L^2((0,t))}^2,$$

where β is a given regularization parameter [18].

This minimization can be efficiently solved, e.g., by applying a standard central

finite difference scheme to its equivalent one-dimensional elliptic equation:

$$(4.6) \quad -\beta \partial_s^2 \Gamma(s) + \Gamma(s) = \Gamma_{\text{prior}}^{\text{recon}}(s), \quad \partial_s \Gamma(0) = \partial_s \Gamma(t) = 0.$$

We denote the minimizer (the regularized version of $\Gamma_{\text{prior}}^{\text{recon}}$) as $\Gamma_{\text{prior,reg}}^{\text{recon}}$.

We would like to emphasize that we are not suggesting solving the original inverse problem with a minimization of a least-squared residual functional because such a method is highly unstable and slow, owing to the high nonlinearity of the functional as well as the high dimensionality of the problem. Instead, the regularization step (4.5) is only to smooth the curve $\Gamma_{\text{prior}}^{\text{recon}}$, which is already obtained from the index function computed by the previous procedures.

This regularized reconstruction provides a smooth and stable estimate of the trajectory of each exact inclusion, as confirmed in the numerical experiments in the next section.

5. Numerical experiments. In this section, we shall present several numerical examples to illustrate the effectiveness of the newly proposed DSM method for the potential identification in the heat equation.

We will take the computing domain $G = [-2, 2]^2$ and set the absorption coefficient and the potential of the homogeneous background to $a = 0.01$ and $q_0 = 0$, respectively, in \mathbb{R}^2 . We then consider the sampling region as the unit ball $\Omega = B_0(1)$. In each of the following examples, there are some moving inhomogeneous inclusions placed inside Ω , with their potential coefficients always set to $q = 5$. The objects B in motion are always set as balls of radius 0.025. Our choice of measurement surface Γ is $\Gamma = \partial\Omega = \mathbb{S}^1$.

In order to collect our observed data of the forward problem, we solve (1.1) with the standard Crank–Nicolson scheme with a fine mesh of size 0.02 in space (namely with 200 grid points in each direction) and 0.025 in time and a first-order absorbing boundary condition on ∂G to model the heat equation in the free space, with initial condition u_0 as

$$u_0(x, y) = 3 + \sin(5x) \cos(5y), \quad (x, y) \in G,$$

and a given final time T to be specified in each example.

The scattered field $f_s := f - f_0$ is then measured along Γ . We emphasize that, for all our subsequent examples, we collect the scattered potential only from a single set of boundary measurement for our reconstruction. Together with the diffusive nature of the forward problem, the resulting inverse problem is severely ill posed.

In order to test the robustness of our reconstruction algorithm, we introduce some multiplicative random noise in the scattered potential as follows:

$$(5.1) \quad f_s^\delta(x, t) = f_s(x, t)(1 + \varepsilon \Delta(x, t)),$$

where Δ is uniformly distributed between -1 and 1 and ε corresponds to the noise level in the data, which is always set to $\varepsilon = 5\%$ in all our examples.

From the noisy observed data f_s^δ , we then use our DSM method as in Algorithm II to recover the moving potential (1.3) by calculating the time-dependent index function \hat{I}_1^2 introduced in (4.3), which is a stabilized version of \hat{I}_1^2 introduced in (3.8). The stabilization procedure for obtaining \hat{I}_1^2 follows the descriptions in section 4.1 with a threshold C to be specified in each example. The mesh size in our reconstruction process is chosen to be 0.025.

As explained in section 4.2, we locate each inclusion by the center of mass of each cluster \hat{I}_1^2 , and our index function is not accurate for an initial period, and the diffusion equation is forward-propagating and we do not have information of the heat distribution before $t < 0$ to give enough information for the location of the inclusions. Indeed, we observe from our numerical experiments that the index is very unstable with noise and jumping around for $t < 0.5$. Therefore, we follow the stabilization procedures described in section 4.2 to obtain $\Gamma_{\text{prior,reg}}^{\text{recon}}(t)$ from \hat{I}_1^2 for each inclusion in each example, with the prior parameter λ and regularization parameter β to be specified.

We recall that the stabilization procedures make use of the following prior knowledge: the inclusions never pass through the center $(0, 0)$ of the domain, and the initial positions of the inclusions are known.

Example 1. In this example, we consider a curve of the form

$$(5.2) \quad \Gamma(t) = \left(\frac{t}{8T} + 0.25 \right) \left(\cos\left(\frac{t\pi}{3}\right), \sin\left(\frac{t\pi}{3}\right) \right), \quad t \in (0, T),$$

which represents the motion of an object inside Ω with the terminal time $T = 5$; see Figure 5 (green curve).

The reconstructed images from the index \hat{I}_1^2 at different times t are presented in Figure 5. The truncation parameter is chosen as $C = 85\%$, and the current location of the inclusion is marked with a yellow star. The trajectory of the reconstructed inclusion is given by the yellow curve, with the prior parameter $\lambda = 1$ and regularization parameter $\beta = 0.05$. A magenta circle is drawn from the center of the yellow star with a radius just to enclose the cluster representing the reconstructed inclusion. From the figure, we can see that with this appropriate cut-off, the exact location of the inclusion is always located near the point marked by the yellow star as the center of mass of the reconstructed inclusion. Although there is always a time lag between the reconstructed inclusion and the exact one, it is surprising that the reconstructed trajectory closely follows that of the exact trajectory from $t = 1$ onward.

As our analyses in sections 3.6 and 3.7 demonstrated, the original index function \hat{I}_0^2 may present a more delayed time in its reconstructed trajectories than the index \hat{I}_1^2 . To verify this, we have run the numerical reconstructions by \hat{I}_0^2 also for Example 1 and listed the results in Figure 6. Comparing the reconstructions by \hat{I}_1^2 (Figure 5) and by \hat{I}_0^2 (Figure 6), we can see the obvious difference in their delay effects. The reconstructed trajectories by \hat{I}_0^2 show a significant delay, and it appears they are moving in less than half the speed as the exact ones. These comparisons have shown the clear outperformance of \hat{I}_1^2 over \hat{I}_0^2 .

Example 2. In this example, we consider another curve of the form

$$(5.3) \quad \Gamma(t) = \left(-\frac{t}{5} + \frac{1}{2} + \frac{1}{40} \cos(t\pi), -\frac{t}{20} + \frac{2}{3} - \frac{1}{0} \cos(t\pi) \right), \quad t \in (0, T),$$

which represents the motion of an object inside Ω with the terminal time $T = 5$; see Figure 7 (green curve).

The reconstructed images from the index \hat{I}_1^2 at different times t are presented in Figure 7. The truncation, prior, and regularization parameters C , λ , and α are set to 85%, 1, and 0.05, respectively. The current location of the inclusion is marked with

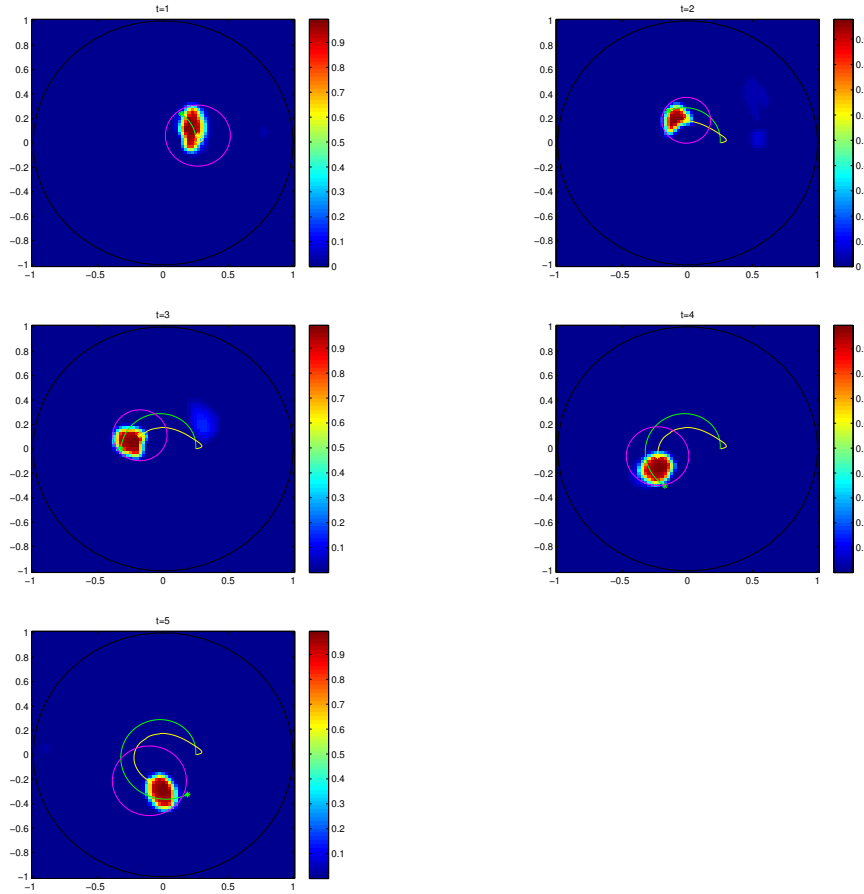


FIG. 5. Reconstructed inclusion from the index \hat{I}_1^2 and trajectories at $t = 1, 2, \dots, 5$ in Example 1. Green curve: exact $\Gamma(0, t)$; green star: exact $\Gamma(t)$. Yellow curve: reconstructed $\Gamma_{prior, reg}^{recon}(0, t)$; yellow star: reconstructed $\Gamma_{prior, reg}^{recon}(t)$. Color is available online only.

a yellow star, and the trajectory of the reconstructed inclusion is given by the yellow curve. A magenta circle is drawn from the center of the yellow star with a radius just to enclose the cluster representing the reconstructed inclusion.

From the figure, we can see that, at the initial period, say for $t < 2$, the reconstructed inclusion tries to find the exact inclusion. Although the signal is sometimes quite weak and the reconstructed inclusion is not always apparent, the reconstruction result is still quite satisfactory. Once it succeeds in approaching the exact inclusion for $t > 2$, it starts to follow the exact path and traces it. The recovered trajectory can even follow some very fine turnings as in the exact one from $t > 4$ onwards.

This is a quite challenging example since the trajectory of the exact inclusion is itself quite oscillatory. In fact, as stated in section 1, theoretically speaking, a time-dependent potential $q(x, t)$ can be uniquely determined by the full lateral Dirichlet-to-Neumann map, i.e., $\Lambda : (u(\cdot, 0), u|_{\Gamma \times (0, T)}) \mapsto (u(\cdot, T), \partial_n u|_{\Gamma \times (0, T)})$. Therefore, one single incidence of $u|_{\Gamma \times (0, T)}$ is far from sufficient to uniquely determine q , not to say that it guarantees any stable reconstruction process. However, it is quite surprising

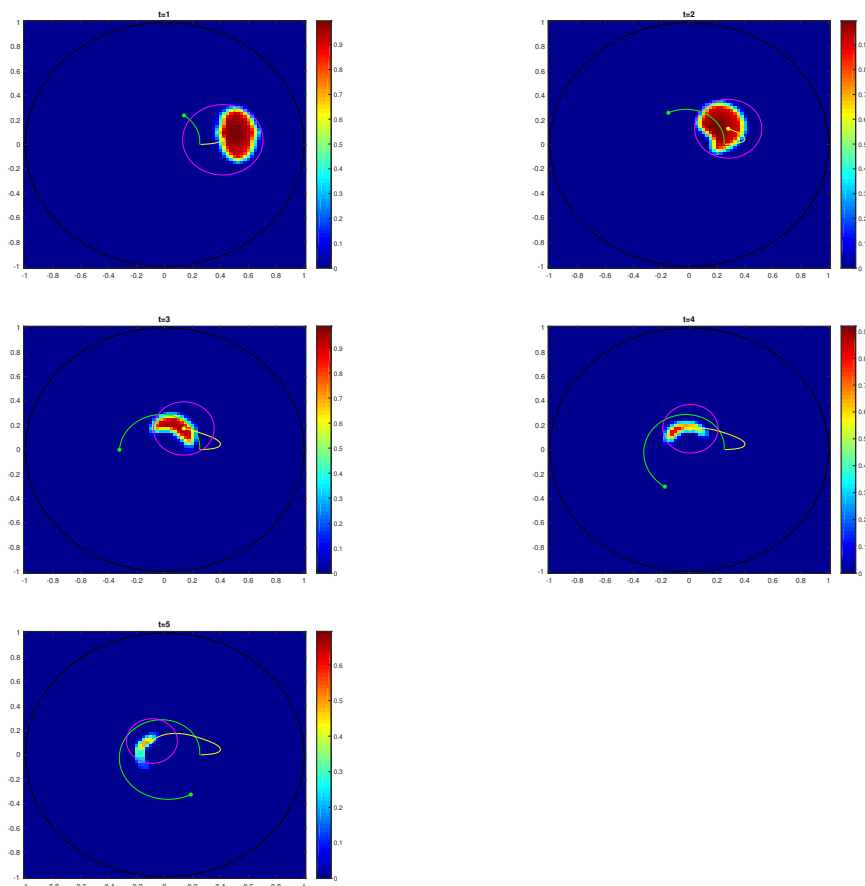


FIG. 6. Reconstructed inclusion from the original index \hat{I}_0^2 (without temporal derivative) and trajectories at $t = 1, 2, \dots, 5$ in Example 1. Green curve: exact $\Gamma(0, t)$; green star: exact $\Gamma(t)$. Yellow curve: reconstructed $\Gamma_{prior,reg}^{recon}(0, t)$; yellow star: reconstructed $\Gamma_{prior,reg}^{recon}(t)$. Color is available online only.

that the reconstruction results by a DSM seem to be very promising in the sense that the reconstructed path follows the exact one from $t > 2$ onward very well. This is indeed a promising result, considering the fact that the measurement is so far from sufficient to even locate the inhomogeneities theoretically.

In order to demonstrate the importance and necessity of the stabilization, we have run the numerical reconstructions by \hat{I}_1^2 (Algorithm I without stabilization) also for Example 2 and listed the results in Figure 8. Comparing the reconstructions by \hat{I}_1^2 (Figure 7) and by \hat{I}_1^2 (Figure 8), the reconstructions by \hat{I}_1^2 are more sensitive to noise, as it may recover some false inclusion components from time to time; e.g., it has a total of four inclusion components at $t = 3$. This is because the previous time frames are not taken into account by the index \hat{I}_1^2 , and therefore it is difficult to screen the constructed inclusions that are inconsistent with a previous time frame. The consequences of the false inclusion components may lead to a serious misjudgment of the true moving target in applications.

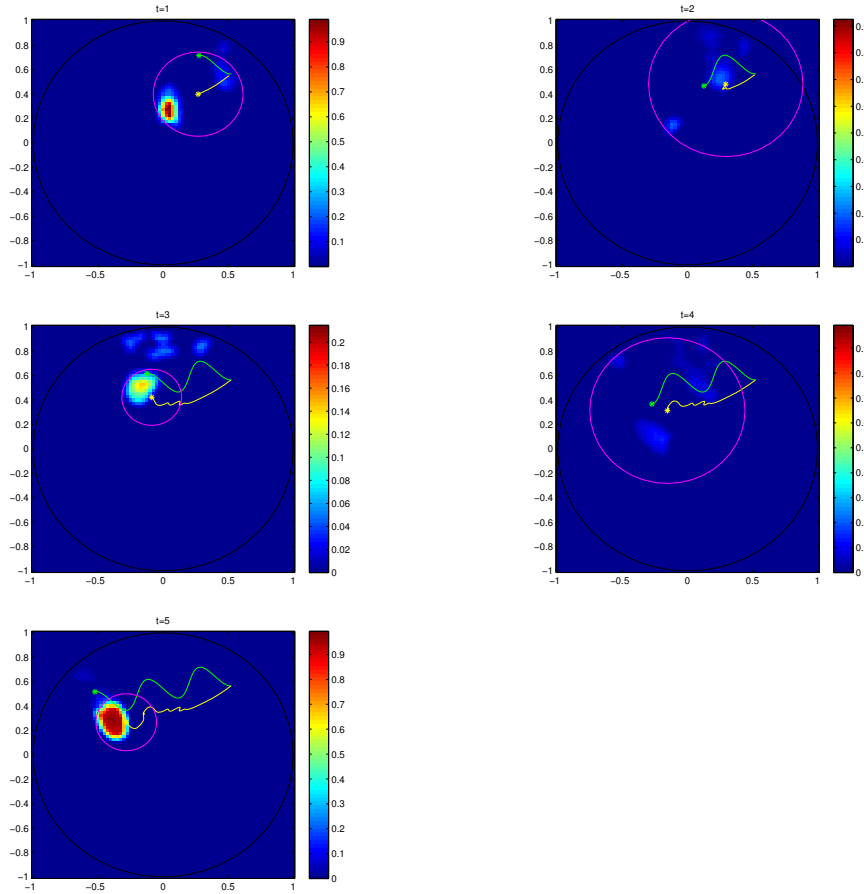


FIG. 7. Reconstructed inclusion from the index \hat{I}_1^2 and trajectories at $t = 1, 2, \dots, 5$ in Example 2. Green curve: exact $\Gamma(0, t)$; green star: exact $\Gamma(t)$. Yellow curve: reconstructed $\Gamma_{prior,reg}^{recon}(0, t)$; yellow star: reconstructed $\Gamma_{prior,reg}^{recon}(t)$. Color is available online only.

Example 3. In this example, we consider two curves given by

$$(5.4) \quad \Gamma_1(t) = \left(\frac{2}{3} \cos\left(\frac{t\pi}{10}\right), \frac{1}{2} \sin\left(\frac{t\pi}{10}\right) \right), \quad t \in (0, T),$$

$$(5.5) \quad \Gamma_2(t) = \left(-\frac{2}{3} \cos\left(\frac{2t\pi}{15}\right), -\frac{1}{2} \sin\left(\frac{2t\pi}{15}\right) \right), \quad t \in (0, T),$$

which represent the motions of two objects inside Ω with a terminal time $T = 7$; see Figure 9 (green curves).

The reconstructed images from the index \hat{I}_1^2 at different times t are presented in Figure 9. The truncation parameter is set to $C = 70\%$, and the current locations of the inclusions are marked by two yellow stars. The trajectories of the reconstructed inclusions are described by two yellow curves, with the prior and regularization parameters $\lambda = 1/2$ and $\beta = 0.1$, respectively. Magenta circles are drawn from the centers of two yellow stars with radii just to enclose the reconstructed inclusions.

From the plots in Figure 9, we can see that from $t = 1$ to $t = 2$, the reconstructions

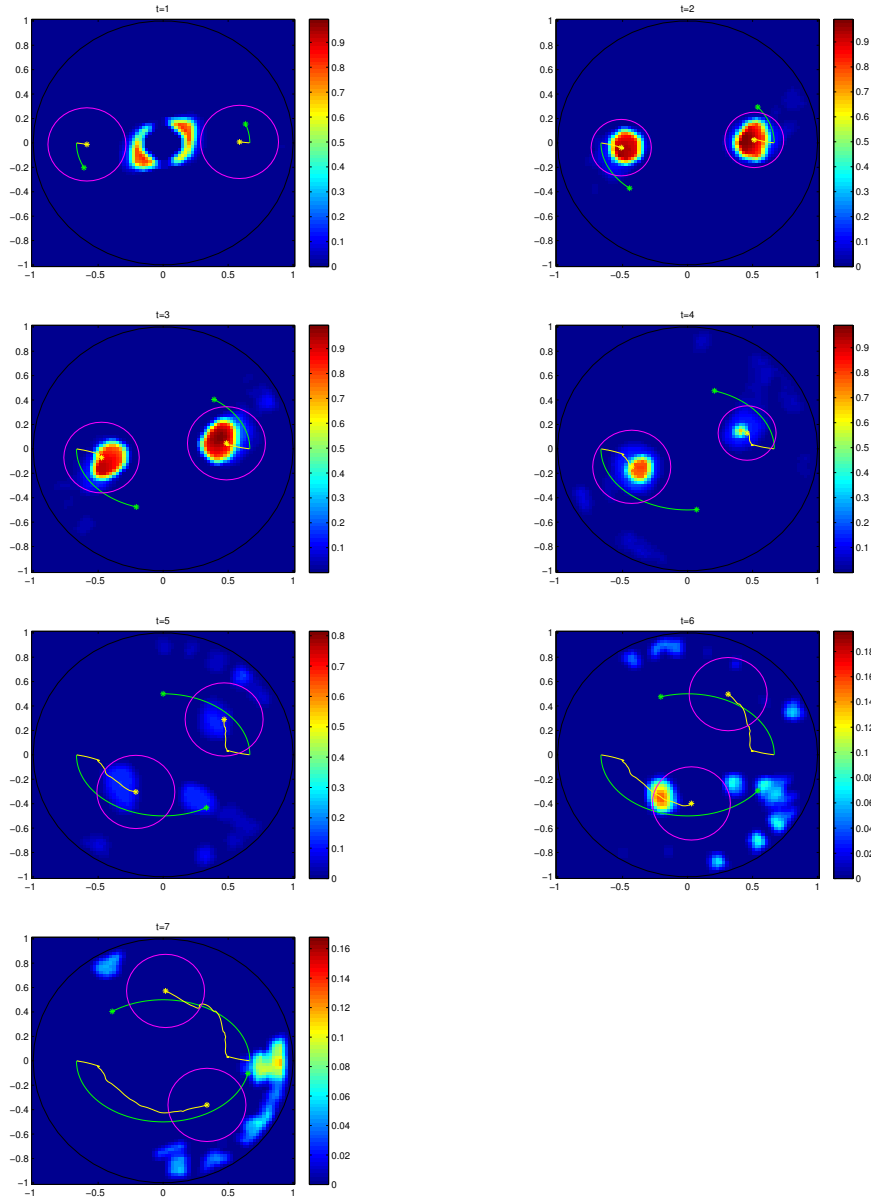


FIG. 9. Reconstructed inclusions from the index \hat{I}_1^2 and trajectories at $t = 1, 2, \dots, 5$ in Example 3. Green curve: exact $\Gamma_i(0, t)$, $i = 1, 2$; green star: exact $\Gamma_i(t)$, $i = 1, 2$. Yellow curves: reconstructed $\Gamma_{i,prior,reg}^{recon}(0, t)$, $i = 1, 2$; yellow star: reconstructed $\Gamma_{i,prior,reg}^{recon}(t)$, $i = 1, 2$. Color is available online only.

period with the dominance of noise, while there are some other time periods when they form fragments. Generally, we can still see the trajectories try to trace the moving inclusions up to time $t = 7$, but the curve starts to oscillate around the exact trajectories due to the disturbance by noise.

This is indeed a very challenging example since we are aiming to simultaneously

locate two objects moving with different velocities in a severely ill posed inverse problem, with only a single set of boundary measurements. Considering the fact that the measurement data is so far from sufficient to uniquely determine q theoretically speaking (not to say so far from a possible stable reconstruction), it is quite surprising that the reconstruction results by a DSM can still locate the two objects with considerable accuracy. In view of these facts, we find the reconstructed trajectories quite encouraging.

REFERENCES

- [1] H. AMMARI AND H. KANG, *Polarization and Moment Tensors: With Applications to Inverse Problems and Effective Medium Theory*, Appl. Math. Sci. 162, Springer-Verlag, New York, 2007.
- [2] H. AMMARI AND H. KANG, *Reconstruction of Small Inhomogeneities from Boundary Measurements*, Lecture Notes in Math. 1846, Springer-Verlag, Berlin, 2004.
- [3] S. A. AVDONIN, M. I. BELISHEV, AND YU. ROZHKOV, *The BC-method in the inverse problem for the heat equation*, J. Inverse Ill-Posed Probl., 5 (1997), pp. 309–322.
- [4] S. A. AVDONIN, S. LENHART, AND V. PROTOPOPESCU, *Determining the potential in the Schrödinger equation from the Dirichlet to Neumann map by the boundary control method*, J. Inverse Ill-Posed Probl., 13 (2005), pp. 317–330.
- [5] H. BEGEHR, *Biharmonic Green functions*, Le Mathematique, 61 (2006), pp. 395–405.
- [6] M. I. BELISHEV, *Canonical model of a dynamical system with boundary control in inverse problem for the heat equation*, Algebra i Analiz, 7 (1995), pp. 3–32 (in Russian); St. Petersburg Math. J., 7 (1996), pp. 869–890 (in English).
- [7] H. BEN OMRANE AND S. KHENISSY, *Positivity preserving results for a bi-harmonic equation under Dirichlet boundary conditions*, Opuscula Math., 34 (2014), pp. 601–608.
- [8] D. A. BOAS, D. H. BROOKS, E. L. MILLER, C. A. DIMARZIO, M. KILMER, R. J. GAUDETTE, AND Q. ZHANG, *Imaging the body with diffuse optical tomography*, IEEE Signal Process. Mag., 18 (2001), pp. 57–75 .
- [9] T. BOGGIO, *Sulle funzioni di Green d'ordine m* , Rend. Circ. Mat. Palermo, 20 (1905), pp. 97–135.
- [10] A. BOUMENIR AND V. K. TUAN, *An inverse problem for the heat equation*, Proc. Amer. Math. Soc., 138 (2010), pp. 3911–3921.
- [11] Y. T. CHOW, K. ITO, K. LIU, AND J. ZOU, *Direct Sampling Method for Diffusive Optical Tomography*, preprint, <https://arxiv.org/abs/1410.1275>, 2014.
- [12] Y. T. CHOW, K. ITO, AND J. ZOU, *A direct sampling method for electrical impedance tomography*, Inverse Problems, 30 (2014), 095003.
- [13] A. DALL'ACQUA, C. MEISTER, AND G. SWEERS, *Separating positivity and regularity for fourth order Dirichlet problems in 2d-domains*, Analysis (Munich), 25 (2005), pp. 205–261.
- [14] S. FANTINI, M. A. FRANCESCHINI, AND E. GRATTON, *Effective source term in the diffusion equation for photon transport in turbid media*, Appl. Opt., 36 (1997), pp. 156–163.
- [15] H.-C. GRUNAU AND F. ROBERT, *Positivity issues of biharmonic Green's function under Dirichlet boundary conditions*, Arch. Ration. Mech. Anal., 195 (2010), pp. 865–898.
- [16] V. ISAKOV, *Inverse Problems for Partial Differential Equations*, Appl. Math. Sci. 127, Springer-Verlag, New York, 2006.
- [17] V. ISAKOV, *On uniqueness in inverse problems for semilinear parabolic equations*, Arch. Rational Mech. Anal., 124 (1993), pp. 1–12.
- [18] K. ITO AND B. JIN, *Inverse Problems: Tikhonov Theory and Algorithms*, World Scientific, Hackensack, NJ, 2014.
- [19] K. ITO, B. JIN, AND J. ZOU, *A direct sampling method for inverse electromagnetic medium scattering*, Inverse Problems, 29 (2013), 095018.
- [20] K. ITO, B. JIN, AND J. ZOU, *A direct sampling method to inverse medium scattering problem*, Inverse Problems, 28 (2012), 025003.
- [21] J. LI AND J. ZOU, *A direct sampling method for inverse scattering using far-field data*, Inverse Probl. Imaging, 7 (2013), pp. 757–775.
- [22] B. D. LOWE AND W. RUNDELL, *The determination of a coefficient in a parabolic equation from input sources*, IMA J. Appl. Math., 52 (1994), pp. 31–50.
- [23] R. POTTHAST, *A study on orthogonality sampling*, Inverse Problems, 26 (2010), 074015.
- [24] A. G. RAMM, *An inverse problem for the heat equation*, J. Math. Anal. Appl., 264 (2001), pp. 691–697.